# Hydrodynamical studies of Quark Gluon Plasma:

## Collective behaviour, initial fluctuations and theoretical fundaments

Astrid Marie Skålvik


Master of Physics

University of Bergen
Department of Physics and Technology
May 2012

Supervisor: Prof. László P. Csernai

# Abstract

This master thesis focuses on collective behaviour of the Quark Gluon Plasma, created at the Large Hadron Collider at CERN.

We calculate analytically and semi-analytically the transverse momentum and rapidity dependence of the flow components $v_1$ and $v_2$. The most important result here is that the global flow component $v_1$ is predicted to no longer peak at negative rapidities for the LHC energies, due to a rotational effect from the initial angular momentum of the system. However, this will be overshadowed by initial state fluctuations of the center of mass rapidity, that appear as the positions of the nucleons fluctuate in the transverse plane. This smoothing out by initial state fluctuations is then included in the expressions of $v_1$ and $v_2$.

Then we investigate how the Time Projection Chamber (TPC) and the Zero Degree Calorimeter (ZDC) detector limitations will distort the measures of the center of mass rapidity $y_{CM}$ and pseudorapidity $\eta_{CM}$ . We show how it is possible to simulate the system after a 1.38 + 1.38 A·GeV Pb + Pb collision with an impact parameter $b = 0.5b_{max}$. The post-collision particles were assumed to follow a pion-Jüttner distribution, emitted from a single or several thermal sources at temperature $T = 0.1$ GeV. The TPC detector limitation of pseudorapidity $\eta < 0.9$ is then taken into account. We also model the ZDC detector response by implementing in our simulation that the ZDC can only detect single neutrons, as charged fragments are deflected by magnetic fields. The TPC and ZDC will then report a $y_{CM}$ that is only a fraction of what would be detected by an ideal Large Array Detector (LAD). The conclusion is that the detector distortions have to be taken into account to avoid underestimating the $y_{CM}$. We also provide a graph showing the expected $y_{CM}^{ZDC}$ vs $\eta_{CM}^{TPC}$ as this could later be compared to experimental data.

# Acknowledgements

I am very grateful for the help and support of my supervisor Professor László P. Csernai. He always took the time to talk with me, discuss my problems and answer my questions. Most importantly, he treated me from the very start as an equal co-worker, therefore giving me the self-confidence to continue with my thesis.

I would also like to thank Alexandre Vial for his technical, academical and motivational assistance. Finally I thank my mother Rannveig Signora Skålvik for her support, and that she now and then made me leave my computer, to take a walk in the mountains and rest my brain.

Bergen, May 2012

# Glossary

| | |
|---|---|
| $b$ | impact parameter |
| $\eta$ | pseudorapidity |
| $\phi$ | azimuth angle |
| $p_\perp$ | transverse momentum |
| $T$ | temperature |
| $v_1$ | global flow component |
| $v_2$ | elliptic flow component |
| $y$ | rapidity |

| | |
|---|---|
| LAD | Large Acceptance Detector |
| LHC | Large Hadron Collider |
| QGP | Quark Gluon Plasma |
| TPC | Time Projection Chamber |
| ZDC | Zero Degree Calorimeter |

# Contents

# Chapter 1

# Introduction

## Significance of the subject

As theoretical physics becomes more and more specialized, it is more important than ever to not lose track of the role every small bit of research plays in the big picture. This thesis focuses on the collective behaviour of quark-gluon-plasma (QGP) created in a heavy-ion collision in the Large Hadron Collider (LHC) at CERN, Switzerland. This experiment recreates the properties of the Universe between $10^{-12}$s to $10^{-6}$s after the Big Bang. A better understanding of the behaviour of the QGP as we find it in LHC will therefore give us precious information about how the Universe acted in the very very beginning of time.

Quarks and gluons are elementary particles that together make up hadronic matter. Baryons are hadrons that are made up of three quarks, like the everyday proton or neutron, whereas mesons are made up of one quark and one antiquark. Under ambient temperature and pressure, the quarks and gluons are held tightly together by the strong nuclear force, which is hundred times stronger than the electromagnetic force and as much as $10^{40}$ times stronger than the Gravitational Force. However, the Strong Nuclear Force is restricted to subatomic distances, thus confining quarks and gluons together in hadrons. Due to a characteristic of this force called the "Asymptotic Freedom", the strength of this force diminishes when the energy increases [1]. Thanks to the extreme energy density created in a heavy ion collision at the LHC, these tight bounds are broken and the free quarks and gluons float around each other in a plasma state. After a short span of time known as the freeze-out time, these elementary particles recombine and there are no more free quarks or gluons.

This recombination happens so fast that it is impossible to measure the existence and the properties of the plasma directly. Therefore the experiments are designed so that they measure collective properties of the matter after the freeze-out time, and we then have to calculate indirectly how the

plasma-state has influenced these final observables.

It is possible to work with these collisions in a number of ways, attacking them from different angles. The theoretical physics team at University of Bergen uses the hydrodynamic approach, and it is this approach that I used in my master project. As will be further explained in chapter 2 concerning the theoretical framework of the hydrodynamic model, we use certain conservation laws and approximate distributions to predict the behaviour of the QGP. My contribution has been to program this in a computer program, and thus simulate the QGP after the collision. From this simulation I have retracted certain variables that can be compared directly to the observables measured in the experiments. In order to make these data fit as good as possible, I have to take into account that the detectors at ALICE are not perfect and their imperfection will influence the measures.

## Structure of the thesis

The first part of my thesis is an explanation of the theoretical fundamentals of the physics behind high energy heavy energy ion collisions. I will discuss the basis of the hydrodynamical model, and the assumptions that are made when modelling the system.

Secondly I will give a brief description of the LHC collider experiment, and introduce the Time Projection Chamber (TPC) and the Zero Degree Calorimeter (ZDC) in the ALICE detector. This is imperative for understanding the following simulations.

Then I will explain the significance of the collective flow components $v_1$ and $v_2$, and the controversy which appears between theory and experiment. Using the notion of initial state fluctuations I will try to explain the apparent discrepancy between the theoretical predictions of the rapidity dependence of the $v_1$, and the actual measurements at the LHC. This part of my thesis is based on a talk I gave at the TORIC Network workshop, Crete, September 2011, which again was based on the article *Fluid dynamical prediction of changed $v_1$ flow at energies available at the LHC* [2], published by my supervisor in 2011. I will also use arguments from the article *Flow Components and initial state CM fluctuations* [3], published by my supervisor in 2012 and of which I was a co-author.

After this I will describe the method I used in order to simulate the measures of center of mass rapidity by the TPC and ZDC at the LHC, in order to evaluate to what extent detector properties will distort the measures. In my simulations I will depart from the Jüttner distribution of an ideal pion gas, impose the detector limitations and compare the result with what would have been measured by an Large Acceptance Detector (LAD). This part is mainly based on a still unpublished article I co-wrote with my supervisor in the spring 2012 [4].

In the end I will summarize the knowledge I have aspired during my year as a master student, and suggest areas of further investigation.

I have also included in the annex the publication where I am a co-author, as well as the source code for my simulation.

# Chapter 2

# Theoretical fundamentals

This chapter is based on the textbook *Relativistic Heavy Ion Collisions* [5] by my advisor Prof. László P. Csernai. Here I will give a general presentation of the kinetic theory upon which we have based our calculations. I will first introduce the necessary notations and conventions, and then I will explain why we have chosen to use a hydrodynamical approach to the QGP. The main focus of this chapter, is to show how we can start with the Jüttner distribution function for an ideal pion gas, apply the three fundamental conservation laws across a freeze out (FO) hypersurface, and in the end deduct the characteristics of the QGP.

## 2.1 Notations and conventions

In order to understand the rest of this thesis it is necessary to be familiar with some basic definitions from the field of high energy physics.

### 2.1.1 Natural units

We have chosen to work with a natural unit system where $c = \hbar = 1$

### 2.1.2 Contravariant and covariant 4-vectors

As the energies of the system increase, it is mandatory to use a relativistic approach, and we therefore use a 4-vector to describe each particle, with 3 spatial and one time coordinate:

Contravariant 4-vector: $x^\nu = (t, \vec{r})$,
Contravariant 4-velocity: $u^\nu = (\gamma, \gamma\vec{v})$
Covariant 4-vector: $x^\nu = (t, -\vec{r})$
Covariant 4-velocity: $u_\nu = (\gamma, -\gamma\vec{v})$,
with $\gamma = \frac{1}{\sqrt{1-\vec{v}^2}}$, so that $u^\nu u_\nu = 1$

To pass from a contravariant to a covariant 4-vector and vice versa, we use the metric tensor defined as $g^{\nu\mu} = g_{\nu\mu} = diag(1, -1, -1, -1)$, so that $x^\nu = g^{\nu\mu} x_\nu$.

Many of the measurables after a heavy ion collision can be calculated based on the momentum of the particles. In a 4-vector convention the 4-momentum of a particle is $p^\nu = (p^0, \vec{p}) = (E, \vec{p})$, normalized as

$$p^\nu p_\nu = \sum_\nu (p^\nu p_\nu) = (p^0)^2 - \vec{p}^2 = m^2$$

### 2.1.3 Rapidity

The rapidity is calculated from the components of the momentum and velocity parallel to the beam of the accelerator, as well as the total energy, using this formula:

$$y = \frac{1}{2} \log \frac{E + P_z}{E - P_z} = \arctan v_z$$

This quantity is approximately similar to the velocity at non-relativistic velocities. As the energies of the system increase, the velocity can only approach c, while the rapidity can take all values from $-\inf$ to $+\inf$. This is illustrated by figure 2.1. Due to the mathematical proprieties of the log operator, the rapidities of two systems are additive, and the Lorentz transformation of rapidity $y_1$ in system 1 and $y_2$ in system 2 is $y_1 + y_2$ of the total system!

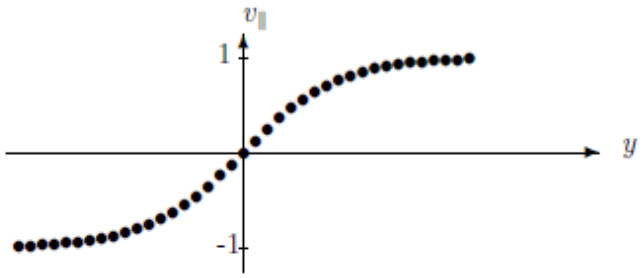


Figure 2.1: The rapidity vs the component of the velocity parallel to the beam [5]

As the energy $E$ of the system can be difficult to measure directly, we also use the *pseudorapidity* $\eta$ which is calculated from the longitudinal momentum and total momentum of the system.

$$\eta = \frac{1}{2} \log \frac{|P| + P_z}{|P| - P_z}$$

For high energies where the kinetic energy is much greater than the rest mass of the projectile, we assume $\eta \approx y$.

### 2.1.4 Particle 4-current

The particle 4-current $N^\mu$ is a macroscopic quantity that can be calculated from the distribution function, and is in other words the 4-vector resulting from combining the particle 4-flow $n(x) = \int d^3p f(x,p)$ and the particle 4-current $\vec{j}(x) = \int d^3p \frac{\vec{p}}{p^0} f(x,p)$

$$N^\mu(x) = \int \frac{d^3p}{p^0} p^\mu f(x,p) = (n(x), \vec{j}(x))$$

### 2.1.5 Energy momentum tensor

The energy momentum tensor $T^{\nu\mu}$ includes the rest mass of the particle as well as the kinetic energy, but does not take into account the action of an external field.

$$T^{\mu\nu} = \int \frac{d^3p}{p^0} p^\mu p^\nu f(x,p)$$

Its components are the following: $T^{00}$ (energy density), $\frac{1}{c}T^{i0}$ (momentum density), $cT^{0i}$ (energy flow) and finally the momentum flow tensor $T^{ik}$ with i and k taking the values 1, 2, 3.

If use $e$ and $P$ for the energy and pressure, then for a perfect fluid in the Local Rest (LR) frame:

$$T^{\mu\nu} = (e+P)u^\mu u^\nu - Pg^{\mu\nu}$$

## 2.2 Hydrodynamical model

There are several ways in which it is possible to model the quark gluon plasma. One well established approach is the non-perturbative Lattice Quantum Chromodynamics. However, due to the complexity of the system involved in the calculation, the Lattice-QCD simulations tend to be overwhelmingly heavy and can only be thoroughly performed using powerful supercomputers.

Therefore we chose to use the hydrodynamical approach when modelling the QGP. The idea behind is to treat the nuclear matter as a continuous medium assumed in local thermodynamic equilibrium, and thus use the equation of motion for ideal fluid dynamics in order to describe the evolution of the system. The QGP is then treated as a fluid in motion, with a certain viscosity, compressibility etc.

### 2.2.1 Relativistic Boltzmann Transport Equation

The relativistic Boltzmann Transport Equation (RBTE) is used to describe the statistical distribution of particles in a non-equilibrium statistical sys-

tem at relativistic energies. It describes the particle conservation in a infinitesimal volume centred around $x$, and a particle with momentum $p$ and distribution function $f$ that collides with a particle with momentum $p_1$ and distribution function $f_1$. The momentum and distribution function after the collision is labelled with a $\prime$.

$$p^\mu \delta_\mu f(x,p) = \frac{1}{2}\int \frac{d^3p_1}{p^0{}_1}\frac{d^3p\prime}{p'^0}\frac{d^3p'_1}{p'^0{}_1}[f\prime f\prime_1 W(p\prime,p\prime_1|p,p_1) - f f_1 W(p,p_1|p\prime,p\prime_1)]$$

Here $\delta_{mu}$ is the 4-derivative, and the distribution function $f$ will be further investigated in the next section.

### 2.2.2 Distribution function of a pion-Jüttner gas

For a heterogeneous system with small gradients, we use the Jüttner distribution as a zero$^{th}$ order approximation for perfect fluid dynamics, also called "Relativistic Boltzmann" distribution, for a particle at point $x$:

$$f_{Juttner}(p) = \frac{1}{(2\,\pi\,\hbar)^3}\exp\frac{\mu(x) - p^\nu u_\nu}{T}$$

where $u_\nu$ is the velocity of the system and $y_0$ is the boost rapidity of the source. $\mu$ is the chemical potential and T is the temperature. For an ideal pion gas the chemical potential $\mu$ equals zero.

### 2.2.3 Freeze out (FO) hypersurface

Due to the high pressure in the colliding fireball, the system will expand. When the particles reach the detector after a collision, they are independent, as the system has expanded until the gas is so diluted that there is no mutual interaction between the particles. This break up or freeze out process is continuous, but when simulating the collision it is more convenient to construct an artificial freeze out hypersurface in the 4-dimensional space time. This hypersurface can be timelike, and its contravariant normal $d\sigma^u$ then points in the time-direction. It can also be spacelike with a co-variant normal, and the freeze out process will therefore happen simultaneously at different places. In the following we will consider a timelike hypersurface. This is illustrated in figure 2.2.

Before reaching the freeze out hypersurface, the particles are interacting according to the laws of fluid dynamics. After the FO, the particles no longer interact, and they can be modelled as an ideal gas. It is also possible to create a more advanced transition, calculating the temperature etc. at each point in space-time, and then impose the FO hypersurface at for example a critical temperature.

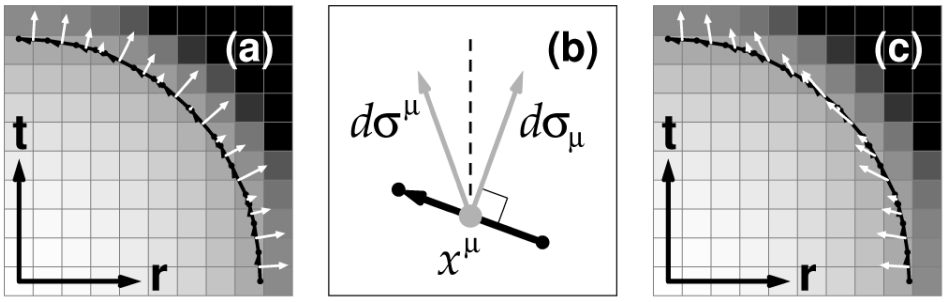


Figure 2.2: From [6]. a) shows the FO hypersurface in a 2-dimensional space-time with a timelike normal. b) shows the timelike and spacelike normal vectors at a space-time point $x^\mu$. c) shows a space-like normal vector.

At the FO instant the particles in the interacting gas all have a certain thermal distribution which has to be accounted with and added to the velocity components of the ideal gas after the transition.

### 2.2.4 Conservation laws across FO

There are certain conservation laws that need to be followed across the FO hypersurface. The particle 4-current $N^\mu$ needs to be conserved, as well as the energy-momentum tensor $T_{\mu\nu}$ (see definitions in sections 2.1.4 and 2.1.5).

In order to verify if the FO hypersurface is physically possible, we calculate the entropy on each side, and if the entropy is decreasing we need to chose a new FO hypersurface.

$$[N^\mu d\sigma_\mu] = 0 \qquad [T^{\mu\nu} d\sigma_\mu] = 0 \qquad dS \geq 0$$

If the proprieties of the interacting fluid is known, then these conservation laws produce a set of equations that can be used to calculate the properties of the ideal non interacting gas after the transition, like temperature $T$, chemical potential $\mu$ and elliptic flow.

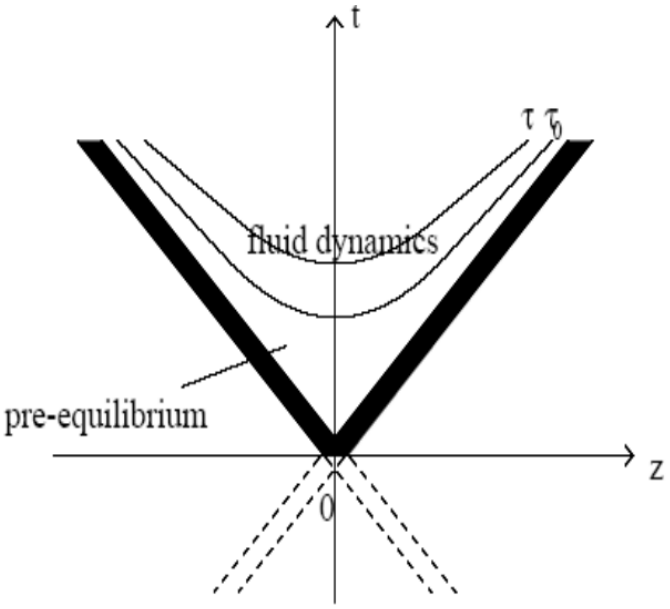


Figure 2.3: The FO hypersurface in a 2D space-time.

## 2.3 Particle in Cell - PIC Hydrodynamical model

The Particle in Cell (PIC) model is used as a tool for numerical simulation of the collision. The system is divided in many cells, where all the particles inside one cell i are randomly generated to follow the distribution function $f(x_i, p)$. As the system evolves and expands, the number of cells filled with matter increases. Since each marker particle carries a fixed charge, the total charge of the system will be conserved during the expansion.

## 2.4 Impact parameter $b$ and centrality

The impact parameter is defined as the distance from the center of the target to the center of the projectile (or the distance between the centers of the two projectiles). If $b = 0$ then the collision is perfectly head on and 100% central. If $b = b_{max}$ then the projectiles did not collide. Collision with $b$ close to $b_{max}$ are called peripheral collisions. See figure 2.4 for illustration.

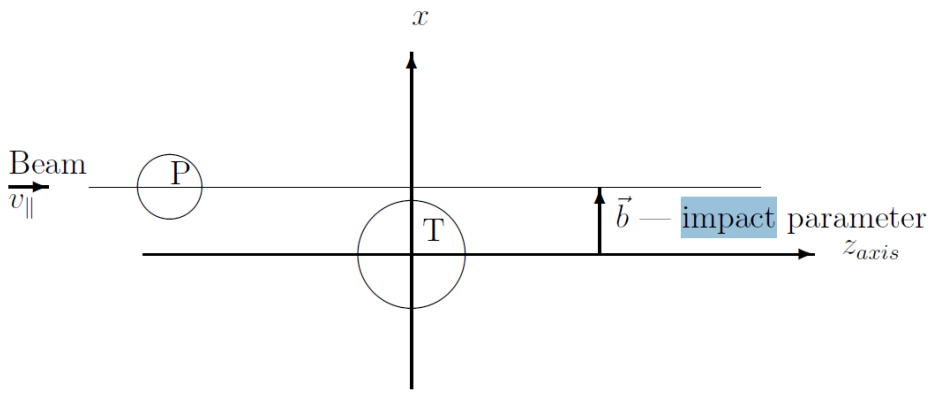


Figure 2.4: Taken from [5]. The impact parameter is perpendicular to the beam direction. P is the projectile, T is the target.

## 2.5 Center of mass rapidity fluctuations $\Delta y_{CM}$

### 2.5.1 Physical explanation

By initial state fluctuations we refer to the event by event fluctuations of the participant nucleon number from projectile and target. These fluctuations may arise from two different mechanisms [2]:

The first is that the particles do not have a fixed position in the participant or transverse plane. Therefore, two similar collisions of Pb+Pb with the same impact parameter, may have different number of nucleons in the participant zone, as the positions of the nucleons are not fixed.

Another reason for the fluctuations may be that even though the projectile nucleons are located in the participant zone, they may avoid colliding with target nucleons, and will therefore become spectators instead of participants.

It is not obvious how to model the initial state. One assumption about our system that will greatly influence the resulting center of mass rapidity fluctuations is to which degree we can consider it to be tightly bound. Is it possible to assume that the extra momentum in one direction or the other may be shared by all the participants that are closely connected, or should we rather let the non-paired nuclei carry this momentum "on their own", without affecting the rest of the participants? If we chose the latter, then there will be a less important change in the collective rapidity. In the following of this thesis, we assume a tightly bound system, as this agrees more with the experimental results for the Pb+Pb reaction at the LHC energy of $1.38 + 1.38$ A·TeV.

### 2.5.2 Calculation of $\Delta y_{CM}$

Assuming a tightly bound system and applying the conservation of momentum, we find that the fluctuating number of participants is connected to the fluctuating center of mass rapidity by the following equation:

$$N_{part} m_N \sinh(\Delta y_{CM}) = \Delta N_{part} m_N \sinh(y_0)$$

Here $N_{part}$ is the number of particles participating in the collision, whereas $m_N$ is the mass of each nucleon. $\Delta y_{CM}$ is the center of mass rapidity fluctuation, and $y_0$ is the rapidity of the beam. Rearranging this equation we get:

$$\boxed{\Delta y_{CM} = arcsinh[\sinh(y_0)\Delta N_{part}/N_{part}]} \tag{2.1}$$

This equation shows that the center of mass rapidity fluctuations will increase for peripheral collisions, where fewer particles will take part in the collision. At these large impact parameters the flow asymmetry is very strong, at the same time there are few participants nucleons. $\Delta y_{CM}$ will also increase with increasing beam rapidities $y_0$, as there will be a stronger impact and each nucleon will carry more momentum.

For a Pb+Pb reaction at $b = 0.7 b_{max}$ collision at the LHC energy of 1.38 + 1.38 A·TeV, assuming a tightly bound system, we can make the following calculation [18]:

If one nucleon from the projectile nucleus is not absorbed into the participant matter, then $\Delta y_{CM} = 1$. For $b = 0.7 b_{max}$, the number of participant nucleons is $N_{part} = 32.7 + 32.7 = 65.4$. For a symmetric collision, the lab frame beam rapidity is $y_0 \approx 8$. We insert this information into equation 2.1 and find $\Delta y_{CM} = 3.8$.

This calculation gives an idea of the importance of understanding and taking into account the initial state fluctuations. We will come back to this analysis in chapters 4 and 5.

## 2.6 Measurables

When modelling the system particle for particle, the measurables are directly calculated from the ideal gas distribution function after the FO hypersurface. Important measurables are the rapidity distribution of the particles, the transverse momentum spectra, the collective flow (ie the elliptic flow) and the average transverse momentum [5].

Chapter 4 of this thesis will discuss more profoundly the rapidity distribution of the particles as well as the collective flow components.

# Chapter 3

# Experimental setup

## 3.1 Large Hadron Collider (LHC) and ALICE at CERN

The Large Hadron Collider (LHC) particle accelerator was built by CERN (the European Organisation for Nuclear Research) between 1998 and 2008, and is designed to investigate the conditions in the universe just after the Big Bang [7]. This is done by colliding two beams of heavy ions at high energies. There are in total 6 detectors connected to this experiment, and this thesis discusses the ALICE detector which focuses on the quark-gluon-plasma state of matter. ALICE stands for A Large Ion Collider Experiment and consists of several sub-detectors, that can be seen in figure 3.1. We will focus on the Time Projection Chamber (TPC) and on the Zero Degree Calorimeter (ZDC), and on the Pb + Pb collision at 1.38 +1.38 A·TeV.

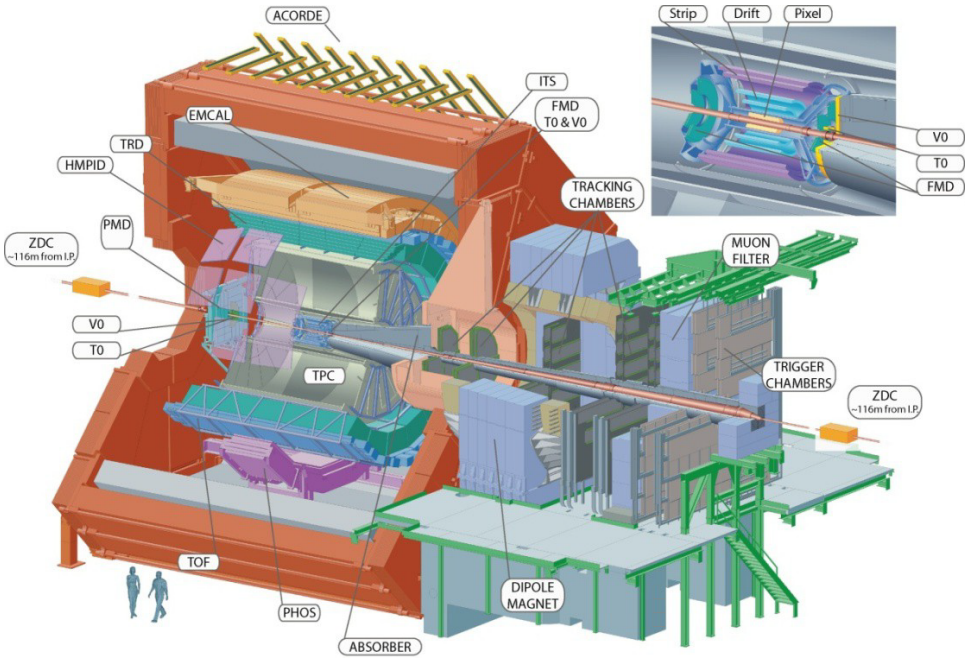


Figure 3.1: A schematic view of the ALICE detector, image from the ALICE collaboration.

## 3.2 Time Projection Chamber (TPC)

The TPC is designed to track charged particles and identify the different kind of particles that are created during the collision. As the particle multiplicity can be very high in a LHC energy Pb + Pb collision, the TPC has to be able to trace many particles simultaneously. It functions in many way as a bubble chamber, where charged particles will ionize gas atoms in the chamber, and the liberated electrons will be attracted towards the anodes of the detector. Here the small electrical signal will be amplified, and read out by 557 568 pads in the multi-wire proportional chambers (MWPC) in the cathode plane [8].

There are two restrictions to the TPC detector. Firstly, it only detects charged particles, as neutral particles will not ionize the atoms in the gas chamber. Secondly, it can only measure particles with $\eta < 0.9$.

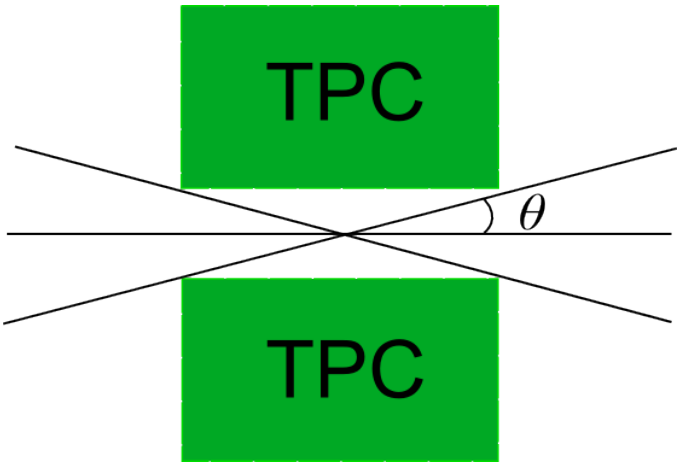


Figure 3.2: Schematic drawing of the rapidity acceptance range of the TPC detector

## 3.3 Zero Degree Calorimeters (ZDC) detector properties

The ZDC detectors are located along the beam line at 115 meters from the interaction point, as can be seen in figure 3.1. They detect the energy of the spectator nucleons, and this information is used to determine the overlap region and to determine if the collision was peripheral or central [9]. It consists of heavy metal plates made of tungsten for detecting neutrons (and brass for detecting protons), surrounded by a matrix of quartz fibres. When neutrons (or protons) hit the brass or tungsten, a shower of particles is emitted, and crossing a fibre this shower will created light, which is converted to an electrical signal using a photomultiplier at the end of the fibre [9]. The amplitude of this signal is proportional to the energy carried by the detected spectators.

The major restriction of the ZDC is that it only detects uncharged neutrons. Charged particles will be deflected away from beam direction by magnetic fields. The fraction of the spectators that are single neutrons depends on the impact parameter of the collision, and the ZDC detected energy will only be proportional to the spectator energy for central collisions. Ref. [10] studies this relation in detail.

# Chapter 4

# Collective flow components $v_1$ and $v_2$

This chapter is based on the article *Flow components and initial state CM fluctuations* [3] published by my supervisor in 2012, and of which I was an co-author, and on the talk *Change of v1 flow at LHC due to rotation* that I gave at the at the TORIC network workshop at Crete in September 2011, which again was based on my supervisors article from 2011, *Fluid dynamical prediction of changed $v_1$ flow at energies available at the LHC* [2].

The constituent quark number scaling with the flow measurements indicates that the collective flow is a result of interactions in the QGP phase, and thus the freeze out happens before the hadronisation of the quarks and gluons [11]. The measurement of the collective flow components will therefore give valuable information about the properties of the quark gluon plasma.

This flow is evidenced by the asymmetric azimuthal distribution around the beam axis:

$$\frac{d^3N}{dydp_td\phi} = \frac{1}{2\pi}\frac{d^2N}{dydp_t}\left[1 + 2v_1(y,p_t)\cos(\phi) + \ 2v_2(y,p_t)\cos(2\phi) + \cdots\right]$$

Here $y$ is the rapidity and $p_t$ is the transverse momentum. $\phi$ designates the azimuth angle in the transverse plane with respect to impact parameter vector, $\vec{b}$ [2]. This is illustrated in figure 4.1.

The functions $v_1$, $v_2$ etc. are the collective flow components. In a perfect fluid with no interaction between its components, after a perfectly symmetric collision, all these collective flow components should equal zero. When the flow components differ from zero, they give us valuable information about the properties of the QGP.

In this chapter we will first find the general analytic expressions for the $p_\perp$ and $y$ dependence of a flow component $v_n$. Then we will apply these

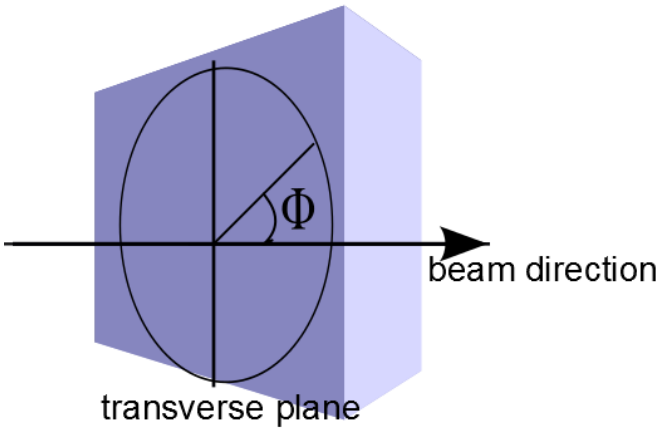


Figure 4.1: $\phi$ is the azimuth angle in the transverse plane with respect to the impact parameter vector, $\vec{b}$

results on the elliptic flow component $v_2$ and the global flow component $v_1$. After that we will introduce the notion of initial state fluctuations from the nucleon positions in the transverse plane, and we will discuss the effect this will have on the flow component. In the end we introduce a new function $v_1^s$ that can be used to separate the contribution of random fluctuations from the global flow.

## 4.1 Flow component calculation

Here we will show how it is possible to use the distribution function of the system after freeze out, together with the Cooper-Frye formula in order to calculate the flow parameters. The first part of the calculations is based on the arguments of [11].

In order to take the kinematic average of a quantity named $C(\vec{x},\vec{p})$, we do the following integrals:

$$\langle C\rangle \;=\; \frac{\int d^3x \int d^3p\; f(\vec{x},\vec{p})\; C(\vec{x},\vec{p})}{\int d^3x \int d^3p\; f(\vec{x},\vec{p})}\,, \tag{4.1}$$

here $f(\vec{x},\vec{p})$ is the distribution function for one particle as introduced in chapter 1. The global flow components $v_1$ and $v_2$ are defined by the following cinematic averages:

$$v_2 \;=\; \left\langle \frac{p_x^2 - p_y^2}{p_\perp^2} \right\rangle \tag{4.2}$$

$$v_1 = \left\langle \frac{p_x}{p_\perp} \right\rangle \tag{4.3}$$

where $p_\perp$ is the transverse momentum: $p_\perp = \sqrt{p_x^2 + p_y^2}$. We can now use the definition of $\phi$ mentioned in the introduction of this chapter together with the identity $\cos 2\,\phi = \cos^2\phi - \sin^2\psi$ to find the following relation: $\cos 2\,\phi = \frac{p_x^2}{p_\perp^2} - \frac{p_y^2}{p_\perp^2}$

The flow components can then be expressed by:

$$v_2 = \left\langle \frac{p_x^2 - p_y^2}{p_\perp^2} \right\rangle = \langle cos(2\phi) \rangle \ , \tag{4.4}$$

$$v_1 = \left\langle \frac{p_x}{p_\perp} \right\rangle = \langle cos(\phi) \rangle \ , \tag{4.5}$$

Inserting these expressions into the above definition of a kinematic average, we get a general formula for the $n_{th}$ flow component as:

$$v_n = \frac{\int d^3x \int_0^{2\pi} d\phi \int_{-\infty}^{\infty} dp_z \int_0^{\infty} dp_\perp p_\perp \ f(\vec{p}) \ \cos n\phi}{\int d^3x \int_0^{2\pi} d\phi \int_{-\infty}^{\infty} dp_z \int_0^{\infty} dp_\perp p_\perp \ f(\vec{p})} \ , \tag{4.6}$$

We can simplify this integral by taking into account our Particle In Cell (PIC) model which was studied in section 2.3. This model distributes the number of particles $N_i$ of our system into $N$ cells with a constant volume $V_i = V_0$ using the distribution function $f_i(\vec{x}, \vec{p})$. Inside a cell $i$ the distribution function does not depend on the $x$ coordinate, and the integral $d^3x$ can therefore be done separately:

$$v_n = \frac{\sum_{i=1}^{N} V_i \int_0^{2\pi} d\phi \int_{-\infty}^{\infty} dp_z \int_0^{\infty} dp_\perp p_\perp \ f^i(\vec{p}) \ \cos n\phi}{\sum_{i=1}^{N} V_i \int_0^{2\pi} d\phi \int_{-\infty}^{\infty} dp_z \int_0^{\infty} dp_\perp p_\perp \ f^i(\vec{p})} \ , \tag{4.7}$$

In order to get an analytic expression for the flow components $v_n(p_t)$ and $v_n(y)$ , we have to make some assumptions: Firstly, we impose a freeze out

hypersurface as described in section 2.2.3. This FO hypersurface is assumed to be constant in time, which means that the transition from quark gluon plasma to the post freeze out gas is happening simultaneously in the whole collision volume. Also, we assume that the particles after the freeze out will only consist of massless pions, and we use the distribution function of an ideal Jüttner gas to describe them:

$$\begin{aligned} f^i_{Juttner}(\vec{p}) &= \frac{1}{(2\,\pi\,\hbar)^3} \exp\left\{\frac{\mu^i - \gamma_i\left(p^i_0 - \vec{p}\vec{v_i}\right)}{T_i}\right\} \\ &= A_i \exp\left\{\frac{-\gamma_i\left(\sqrt{m^2_\perp + p^2_z} - v^i_z p_z\right)}{T_i}\right\} \\ &\quad \times \exp\left\{\frac{\gamma_i p_\perp v^i_\perp cos(\phi - \phi^i_0)}{T_i}\right\} \end{aligned} \tag{4.8}$$

Here $u^\mu_i$ is the flow 4-velocity of the particles in cell $i$. In order to facilitate the calculations, we chose to rewrite its components as:

$$u^\mu_i = \gamma^i(1, v^i_x, v^i_y, v^i_z) = \gamma^i(1, \vec{v^i_\perp}, v^i_z)$$

The normalization factor $A_i$ is defined by:

$$A_i = \frac{1}{(2\pi\hbar)^3}\, exp\left(\frac{\mu^i}{T}\right)$$

As we assume the gas to consist of massless pions, the transverse mass is defined by $m^2_\perp = m^2 + p^2_\perp = p_\perp$ and the chemical potential $\mu^i = 0$, and $A_i$ is therefore a constant for each cell $i$.

### 4.1.1 Transverse momentum dependence of the flow

Equation 4.7 above gives the kinematic average $v_n = \langle cos(n\phi)\rangle$, where the average is taken over the whole configuration space. If we instead want to find the $p_\perp$ dependency of the $v_n$ component, we do not integrate over $p_\perp$, and get:

$$v_n\left(p_\perp\right) = \frac{\sum_{i=1}^{N} V_i \int_0^{2\pi} d\phi \int_{-\infty}^{\infty} dp_z\; f^i(\vec{p})\; \cos n\phi}{\sum_{i=1}^{N} V_i \int_0^{2\pi} d\phi \int_{-\infty}^{\infty} dp_z\; f^i(\vec{p})}, \tag{4.9}$$

We then insert the expression for the Jüttner distribution function as found in section 4.8, and in order to make the equation less charged, we take into account that the volume $V_i$ is constant for each cell, so the factor $\sum_{i=1}^{N} V_i$ will cancel in the nominator and denominator. We also write the component of the momentum which is parallel to the velocity of the cell as $p_v = p_\perp \cos(\phi - \phi_0)$, where $\phi_0$ denotes the angle between the direction of the cell velocity and the $x$-axis. Equation 4.9 then becomes:

$$v_n(p_\perp) = \frac{\int_0^{2\pi} d\phi \int_{-\infty}^{\infty} dp_z \exp[-\gamma_i(\sqrt{m_\perp^2+p_z^2}-v_z^i p_z)/T_i] \exp[\gamma_i p_\perp v_\perp^i cos(\phi-\phi_0^i)/T_i] \cos n\phi}{\int_0^{2\pi} d\phi \int_{-\infty}^{\infty} dp_z \exp[-\gamma_i(\sqrt{m_\perp^2+p_z^2}-v_z^i p_z)/T_i] \exp[\gamma_i p_\perp v_\perp^i cos(\phi-\phi_0^i)/T_i]} \tag{4.10}$$

The denominator (named $V_n(p_\perp)$) of this equation can be written as two separate integrals:

$$V_n(p_\perp) = \int_0^{2\pi} d\phi \cos n\phi \exp \frac{\gamma p_\perp v_\perp cos(\phi-\phi_0)}{T} \int_{-\infty}^{\infty} dp_z \exp \frac{\gamma(v_z p_z - \sqrt{m_\perp^2+p_z^2})}{T}$$

$$\Longrightarrow V_n(p_\perp) = D_n(p_\perp) \cdot B(p_\perp) \tag{4.11}$$

The $D_n(p_\perp)$ integral can be expressed using a Bessel function $I_n$ and is therefore possible to calculate analytically:

$$D_n(p_\perp) = 2\pi I_n(\gamma v_\perp p_\perp/T) cos(n\phi_0)\,, \tag{4.12}$$

The calculation of $B(p_\perp)$ is less straightforward, but possible. We start by separating the expression into:

$$B(p_\perp) = b(p_\perp, v_z) + b(p_\perp, -v_z), \tag{4.13}$$

where $b(p_\perp, v_z)$ is

$$b(p_\perp, v_z) = \int_0^{\infty} dp_z \exp\left\{ \frac{-\gamma\left(\sqrt{m_\perp^2+p_z^2} - v_z p_z\right)}{T} \right\}.$$

Now we can use a change of variables $t = \sqrt{m_\perp^2 + p_z^2} - v_z p_z$ to get

$$b(p_\perp, v_z) = \int_{m_\perp}^{\infty} dt\; e^{-\gamma t/T} \left( \frac{v_z}{1-v_z^2} + \frac{1}{1-v_z^2} \frac{t}{\sqrt{t^2 - m_\perp^2(1-v_z^2)}} \right),.$$

This again can be inserted into equation 4.13, and we get, using a Bessel function $K_1$:

$$B(m_\perp) = \frac{2m_\perp}{\sqrt{1-v_z^2}} K_1\left(\frac{\gamma m_\perp \sqrt{1-v_z^2}}{T}, \frac{\gamma m_\perp}{T}\right) - \frac{2m_\perp |v_z| e^{-\frac{\gamma p_t}{T}}}{1-v_z^2}\,.$$

So, the final, analytic expression for the transverse momentum dependence of the flow is

$$\boxed{v_n\left(p_\perp\right) = \frac{\sum_{i=1}^{N} V_i A_i B(i, m_\perp^i) I_n(\gamma^i v_\perp^i p_\perp / T_i) \cos n\phi_0^i}{\sum_{i=1}^{N} V_i A_i B(i, m_\perp^i) I_0(\gamma^i v_\perp^i p_\perp / T_i)}} \tag{4.14}$$

### 4.1.2 Rapidity dependence of the flow

In order to calculate the rapidity dependence of the flow, let us recall that $p^0 = m_\perp \cosh y$, $p_z = m_\perp \sinh y$, and correspondingly $dp_z = m_\perp \cosh y \; dy$. Then the Jüttner distribution can be rewritten in terms of rapidity as

$$\begin{aligned} f^i_{Juttner}(\vec{p_\perp}, y) &= A_i \exp\left\{-\frac{\gamma_\perp^i m_\perp \cosh\left(y - y_0^i\right)}{T_i}\right\} \\ &\quad \times \exp\left\{\frac{\gamma_\perp^i p_\perp \tilde{v}_\perp^i cos(\phi - \phi_0^i)}{T_i}\right\}, \end{aligned} \tag{4.15}$$

where $y_0^i$ is the flow rapidity, and we have also rewritten the flow 4-velocity in the following way: $u_i^\mu = \gamma_\perp^i(\cosh y_0^i, \sinh y_0^i, \vec{\tilde{v}_\perp^i})$, with $\vec{\tilde{v}_\perp^i} = \vec{v_\perp^i}/\sqrt{1-(v_z^i)^2}$, $\gamma_\perp^i = 1/\sqrt{1-(\tilde{v}_\perp^i)^2}$.

Leaving $y$-dependence in flow definition, (4.7), "unintegrated", we obtain the following equation:

$$v_n\left(y\right) = \frac{\sum_{i=1}^{N} V_i \int_0^{2\pi} d\phi \int_0^{\infty} dp_\perp p_\perp m_\perp \; f^i(\vec{p_\perp}, y) \; \cos n\phi}{\sum_{i=1}^{N} V_i \int_0^{2\pi} d\phi \int_0^{\infty} dp_\perp p_\perp m_\perp \; f^i(\vec{p_\perp}, y)}\,. \tag{4.16}$$

Here the sums over volumes cancel each other out, as explained in the above section, as $V_i = V_0$ is constant for all cells. Unfortunately the $\phi$ and $p_\perp$ integrals do not factorize in eq. (4.16), and only the $\phi$ integral can

be performed analytically. Using eq. (4.12) we obtain the semi-analytic expression of the rapidity dependence of the flow components:

$$\boxed{v_n(y) = \frac{J_n(y, \vec{v}^{\,i}, T^i) cos(n\phi_0^i)}{J_0(y, \vec{v}^{\,i}, T^i)}\,,} \tag{4.17}$$

where

$$\begin{aligned} J_n(y, \vec{v}^{\,i}, T^i) &= \int_0^\infty dp_\perp p_\perp m_\perp I_n(\gamma_\perp^i \tilde{v}_\perp^i p_\perp / T^i) \\ &\quad \times \exp\left\{-\gamma_\perp^i m_\perp \cosh(y - y_0^i)/T^i\right\}\,. \end{aligned} \tag{4.18}$$

## 4.2 $v_2$ collective flow: Elliptic flow

$v_2$ is called the elliptic flow component. $v_2(p_t)$ is observed to be larger at the LHC than at lower energies [12], and thus reveals a strongly interacting quark gluon plasma. The elliptic flow is the transverse expansion in the reaction plane as a result of the almond-shaped initial overlap zone of the projectile and target [13]. In more central collisions, the random initial state fluctuations will overshadow this effect, and it is not possible to measure a significant elliptic flow.

### 4.2.1 Transverse momentum dependence of the elliptic flow

The calculated $v_2(p_t)$ distributions are similar to the experimental trends both in the magnitude and the centrality dependence, especially at the smaller centralities [12]. For illustration one calculated $v_2(p_t)$-distribution is presented in Fig. 4.2 [2].

### 4.2.2 Rapidity dependence of the elliptic flow

The calculated $v_2$ parameter versus the rapidity $y$, using equation 4.16, is shown in Fig. 4.3. As we can see the $v_1$ is relatively large and easily measurable in the experimental rapidity range $|y| \leq 0.9$, reaching a central value approaching the experimental one. This curve is calculated including contributions from all rapidities. The central dip is a consequence of the constant time FO for an ideally symmetric FD initial state [2]. At t=8 fm/c many particles have already left the impact zone. As we will see later random initial state fluctuations smooth out these structures.

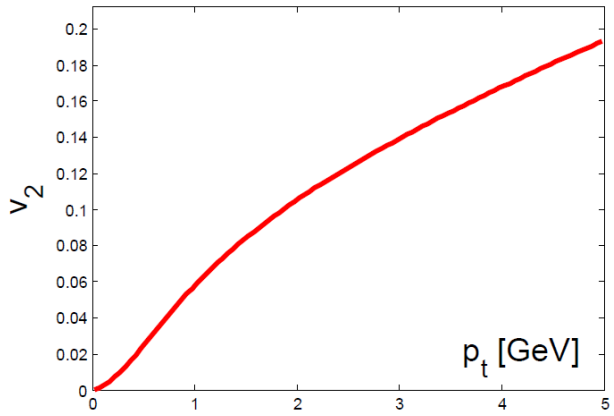


Figure 4.2: From [2]. The $v_2$ versus the transverse momentum $p_t$ for $b = 0.7b_{max}$, at $t = 8$ fm/c FO time. This analytic result is comparable to the experiment for at 40-50 % centrality

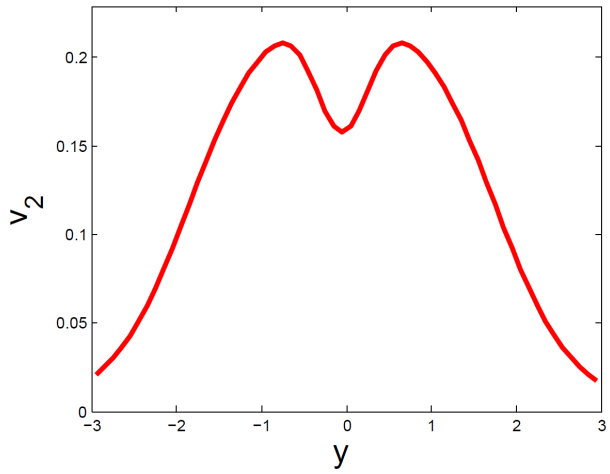


Figure 4.3: From [2] The $v_2$ versus the rapidity, $y$ for $b = 0.7b_{max}$, at $t = 8$ fm/c FO time. The $v_2(y)$ curve shows a local minimum at central rapidity. The local minimum for central rapidity is a result of the constant time FO, as most particles have already left the impact zone.

## 4.3 $v_1$ global collective flow

The $v_1$ component is also named *anti-flow* as it peaked at negative rapidities at SPS and RHIC [14, 15]. However, at higher energies at the LHC, we expect the $v_1$ flow to peak in the positive direction for positive rapidities, and in the negative direction for negative rapidities, and it should thus no longer be an *anti-flow*. The accurate measurement of this flow can help to reveal information about transport properties and the pressure of the QGP [2].

The initial state of the system just after a non-central collision is tilted, and the flow velocity distribution will cause the system to rotate, see figure. 4.4. The direction of the strongest pressure gradient is upwards for backwards moving matter (negative rapidity) and downwards for forward moving matter (positive rapidity), and this suggests a $v_1$ flow that will peak at negative rapidities.

At higher energies, however, the distribution of the flow velocity of the initial state will rotate the system further, and this initial angular momentum will make the strongest pressure gradient rotate to the upward direction for forward moving particles and to the downward direction for backward moving particles before the system freeze out, and the particles finally hit the detectors. This is illustrated in figure 4.5.

### 4.3.1 Transverse momentum dependence of the global collective flow

As $v_1$ is an antisymmetric function of $p_z$ (or $y$), the $p_z$-integrated $v_1(p_\perp)$ value must vanish. In order to still be able to analyse this aspect of $v_1$, we introduce a new, symmetrized function $v_1^s$. This function is constructed by reversing the $p_\perp$ direction of backward going particles before doing the $y$ integral. $v_1^s$ is then a small, but non-vanishing function, and is less sensitive to random fluctuations [16, 2].

$$v_1^S(p_\perp) = \frac{\sum_{i=1}^{N} 2\pi V_i A_i D(i, m_\perp^i) I_n(\gamma^i v_\perp^i p_\perp / T_i) \cos n\phi_0^i}{\sum_{i=1}^{N} 2\pi V_i A_i B(i, m_\perp^i) I_0(\gamma^i v_\perp^i p_\perp / T_i)}, \tag{4.19}$$

where

$$D(i, m_\perp^i) = e^{-\gamma^i m_\perp^i / T^i} \frac{2v_z}{1 - v_z^2} \frac{T^i}{\gamma^i}. \tag{4.20}$$

The trace of $v_1^s(p_\perp)$ is the solid line in figure 4.6.

### 4.3.2 Rapidity dependence of the global collective flow

The analytically calculated $v_1$ parameter versus the rapidity $y$, from equation 4.16 is shown in Fig. 4.7. As we can see the $v_1$ is relatively large and easily measurable in the experimental rapidity range $|y| \leq 0.9$. The most important change with respect to the similar simulations for RHIC [15] is that the $v_1$ now peaks in "forward" direction, i.e., the positive (negative) peak appears now at positive (negative) rapidity.

There are two problems with these predictions. First, the $v_1$ component measured at RHIC was about 5 times smaller than the predicted values from our Fluid Dynamical calculations [2, 17]. Second, the recent measures of the $v_1$-flow at the high energies of the LHC shows that it still peaks in a negative direction , contrary to our predictions. Both of these discrepancies with our theory can be explained by taking into account the *initial state fluctuations* of the system, explained in the following section.

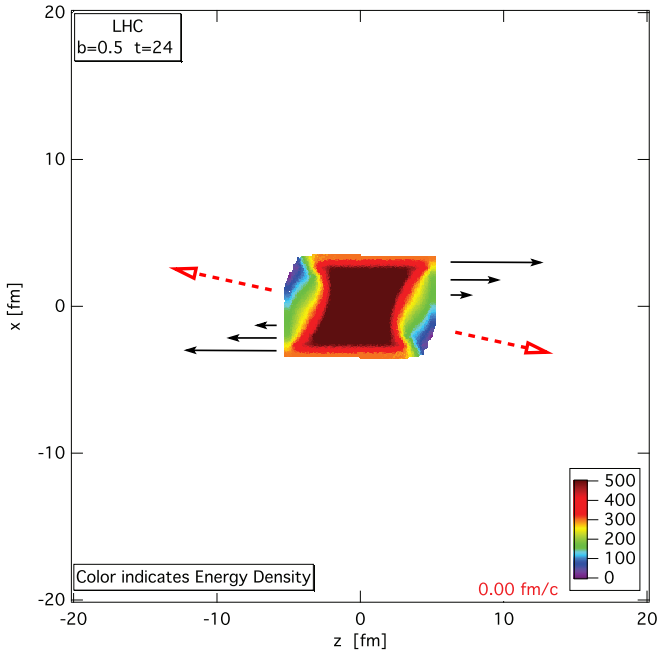


Figure 4.4: From [2]. Initial distribution of the energy density (GeV/fm$^3$) for a 1.38+1.38 A.TeV Pb+Pb collision 4 fm/c after the impact.

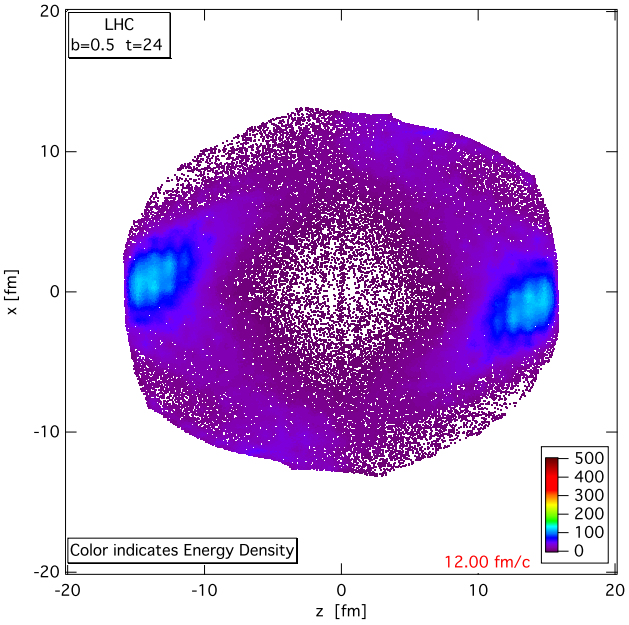


Figure 4.5: From [2]. Distribution of the energy density (GeV/fm$^3$) for a 1.38+1.38 A.TeV Pb+Pb collision 12 fm/c after the impact.

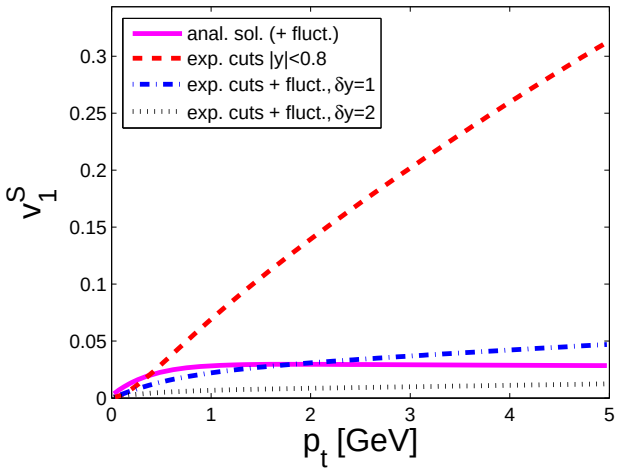


Figure 4.6: From [2]. $v_1^S$ from eq. (4.19) versus the transverse momentum, $p_t$ for $b = 0.7b_{max}$, at $t = 8$ fm/c FO time.

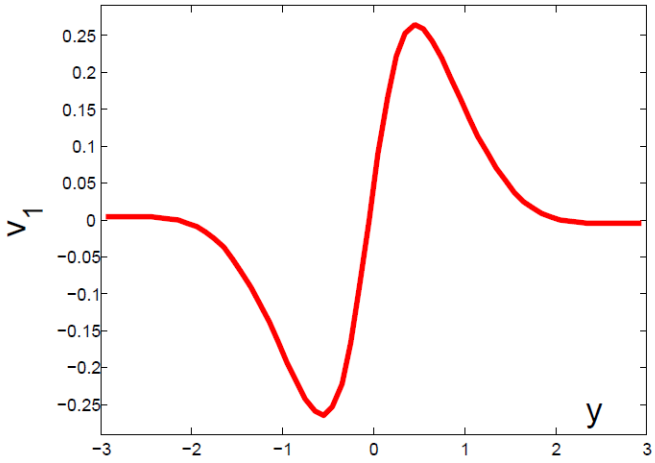


Figure 4.7: From [2]. $v_1$ versus the rapidity $y$ for $b = 0.7b_{max}$, at $t = 8$ fm/c FO time. This is the trace of the semianalytical eq. (4.17); We observe the $v_1$ to peak at positive rapidity, no more anti-flow.

## 4.4 Effect of initial state fluctuations

Here I will explain how our predicted global collective flow may be diminished as well as completely overshadowed by longitudinal initial fluctuations. This section is building on the theoretical fundaments of the initial state fluctuations from section 2.5.

When the initial state fluctuations are not taken into account, there are important discrepancies between the theoretical simulations and the experimental collision data of the global collective flow $v_1$. For lower energies at the SPS and RHIC the fluid dynamical models still predict the $v_1$ to be an *anti-flow*, peaking at negative rapidity values [14, 15]. The position of the peaks agreed with experimental measures, but the peaks were much smaller than the predicted values [14, 17]. At the RHIC for 62.4 + 62.4 and 200 A·GeV, the $v_1$ was measured to be about 5 times smaller than the FD prediction.

We therefore need to update our model.

### 4.4.1 Effect on $y$ dependence

As studied in section 2.5, the center of mass rapidity will have bigger fluctuations in peripheral collisions and at high beam rapidities. Due to the assymetry of $v_1(y)$, these fluctuations will be most important at central rapidities. The $v_1$ changes sharply around $y = 0$, whereas $\Delta y_{CM}$ follows a symmetric distribution centred around $y = 0$. Figure 4.8 illustrates the resulting smoothing effect of these fluctuations.

To analyse the consequences of these longitudinal rapidity fluctuations, we added a rapidity distribution $dy$ to the rapidity of each cell with $< dy >= 0, 1, 2$, so that $y_{CM}$ followed a Gaussian distribution centred at $y_{CM} = 0$ [2]. The case, $dy = 0$, returned the original ideally symmetric fluid dynamical solution, which overestimates the measured or expected data.

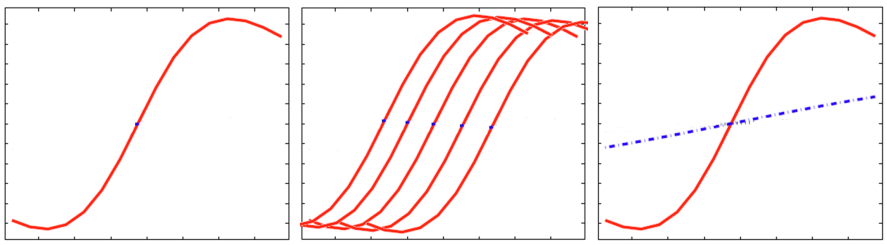

Figure 4.8: The first graph shows $v_1(y)$ when no CM rapidity fluctuations are taken into account. The second graphs shows the $v_1(y)$ traced for different center of mass rapidities. The dotted line in the third graph shows the average of all the different $v_1(y)$ traces. The axis are empty as these graphs are only for illustration, and not to scale.

This leads to the following final expression for the rapidity dependence of the flow components:

$$\boxed{v_n(y) = \frac{\sum_{i=1}^{N} V_i R_n(y, \vec{v}^{\,i}, T^i) cos(n\phi_0^i)}{\sum_{i=1}^{N} V_i R_0(y, \vec{v}^{\,i}, T^i)}}, \tag{4.21}$$

where

$$R_n(y, \vec{v}^{\,i}, T^i) = \frac{1}{\sqrt{2\pi\delta y^2}} \int_{-\infty}^{\infty} dy' \exp\left\{-\frac{(y-y')^2}{2\delta y^2}\right\} \times J_n(y', \vec{v}^{\,i}, T^i) \cosh y'$$

and $J_n(y', \vec{v}^{\,i}, T^i)$ is given by eq. (4.18).

The dash-dotted lines in fig. 4.9 and fig. 4.10 show how the fluctuations reduce $v_1(y)$ at central rapidities and widens out the central dip in $v_2(y)$.

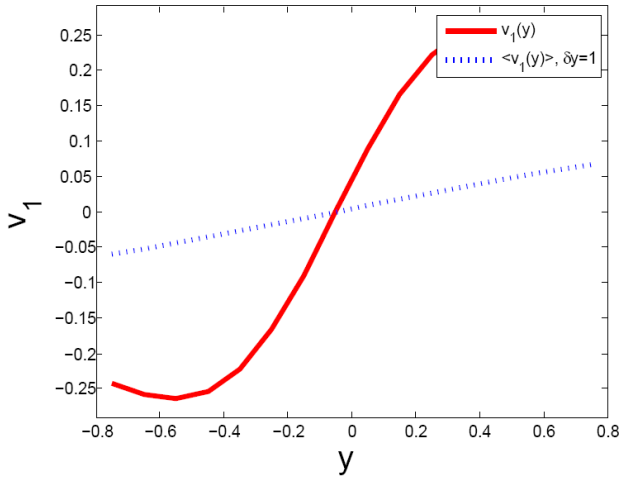


Figure 4.9: From [2]. $v_1$ versus the rapidity $y$ for $b = 0.7b_{max}$, at $t = 8$ fm/c FO time. The solid line is calculated using eq. (4.17), and the dashed line takes into account initial CM rapidity fluctuations.

### 4.4.2 Effect on $p_\perp$ dependence

In principle, there should be no effect of the CM rapidity fluctuations on the transverse momentum dependence of the flow components. This is because we should anyway integrate $y$ from $-\infty$ to $+\infty$. However, this does not apply in realistic situations, as the TPC detector only detects particles whose rapidity is in the range $-0.9 \leq y \leq 0.9$. We therefore have to include this

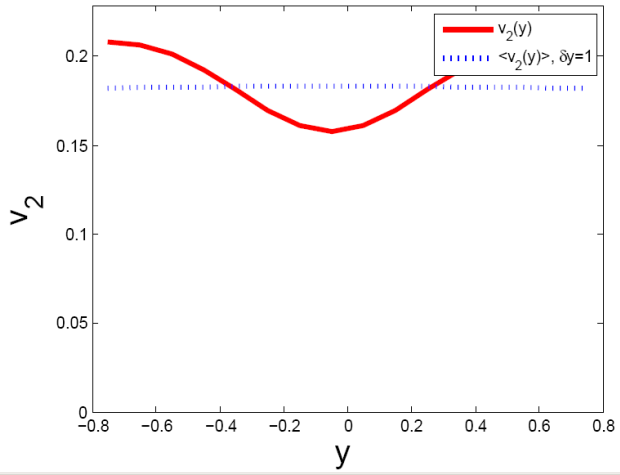


Figure 4.10: From [2]. $v_2$ versus the rapidity $y$ for $b = 0.7b_{max}$, at $t = 8$ fm/c FO time. The solid line is calculated using eq. (4.17), whereas the dotted lines take into account the initial CM rapidity fluctuations.

into our calculations of $v_1^S(p_t)$ and $v_2(pt)$. The coefficient $B(m_\perp^i)$ in our semi-analytic equation 4.14 will therefore change to:

$$B(i,p_\perp) = \frac{m_\perp}{\sqrt{2\pi\delta y^2}} \int_{-0.9}^{0.9} dy \int_{-\infty}^{\infty} dy' \cosh y' \times \exp\left\{-\frac{\gamma_\perp^i m_\perp \cosh\left(y'-y_0^i\right)}{T_i}\right\} \exp\left\{-\frac{(y-y')^2}{2\delta y^2}\right\} \quad (4.22)$$

The predicted effect of these CM rapidity fluctuations on the symmetrised global collective flow can be observed in figure 4.6.

### 4.4.3 Isolating the random fluctuation effect on $v_1$

It is possible to isolate the contribution from random fluctuations on the $v_1$ by separating the $v_1^s$ into odd and even components, as was done in [2]. As $v_1$ is Global Mirror Asymmetric, then all even components should vanish. Therefore, only the initial state random fluctuations can be responsible for any Mirror Symmetric part and a non-zero $v_1(pt)$. Since the initial state fluctuations are random, there should be no difference between its even and odd parts. Ref. [2] then concludes that

$$v_1^{S,odd}(p_\perp) = v_1^{S,fluct}(p_\perp) \quad (4.23)$$

$$v_1^{S}(p_\perp) = v_1^{S,even}(p_\perp) - v_1^{S,odd}(p_\perp) \quad (4.24)$$

The $v_1^S$ function is therefore really useful for analysing the nature of the global collective flow.

# Chapter 5

# TPC and ZDC C.M. rapidity detection

This part of my thesis is based on an unpublished article regarding the TPC and ZDC detector restrictions that I co-wrote with my supervisor the Spring of 2012 [4].

In this chapter we will show how we can simulate the pion gas after the collision and extract from the data the C.M. rapidity and pseudorapidity as it would be measured by the ZDC and the TPC.

It is very interesting to find the correlation between the pseudorapidity detected by the Time Projection Chamber (TPC) and the rapidity detected by the Zero Degree Calorimeter (ZDC). The two detectors have different limitations, and for small rapidities the ZDC is assumed to measure the rapidity without any cut in the rapidity range. However, the ZDC will only detect single neutrons spectators that are not bound in charged nuclear fragments which may be deflected away from the beam direction by the applied magnetic fields. If it is possible to establish a correlation between the rapidity measured by these two detectors, we could estimate the C.M. rapidity of the participants event by event, and identify the impact of random fluctuations in the spectator sizes and energies.

## 5.1 One source

In order to simulate the detection of the particles by the TPC, we generated the momentum of 500 particles following a Jüttner pion distribution.

$$f^i_{Juttner}(p) = \frac{C}{(2\,\pi\,\hbar)^3} \exp \frac{p^\nu_i u_{\nu,i}}{T}$$

We assumed a thermal system with temperature T. $\mu_i$ is the chemical potential of the source cell, $i$, and as an ideal quark gluon plasma is a pion gas, the chemical potential equals zero.

The velocity 4-vector is given by $u_{\nu,i} = (\cosh(y), 0, 0, \sinh(y))$, with no velocity in the transverse direction. Here $y$ designates the boost rapidity of the source which was varied in the longitudinal (z) direction, due to initial state fluctuations of the positions of the nucleons, and thus of the number of participants from the target or the projectile.

As both the TPC and ZDC detectors have detected center of mass rapidity fluctuations not exceeding -0.5 and +0.5 for a 1.38+1.38 A.TeV peripheral collision [18], we have chosen to carry out our simulations in this range.

As the inverse of this equation is not know, we generate the momenta by first taking the integral of the Jüttner distribution, which shows the cumulative distributions of the momenta, going from 0 to 1 (as $f^i$ is normalized to unity [5]). We define

$$g(p_z) = \int_{-\infty}^{\infty}\int_{-\infty}^{\infty}\int_{-\infty}^{p_z} f^i_{Juttner}(p)\, d^3p, \ \ where\ g \in [0,1].$$

Then we generate 500 random numbers between 0 and 1 and find the corresponding momentum for each [19]. The result is 500 momenta following the given Jüttner distribution! See Fig. 5.1 for illustration.

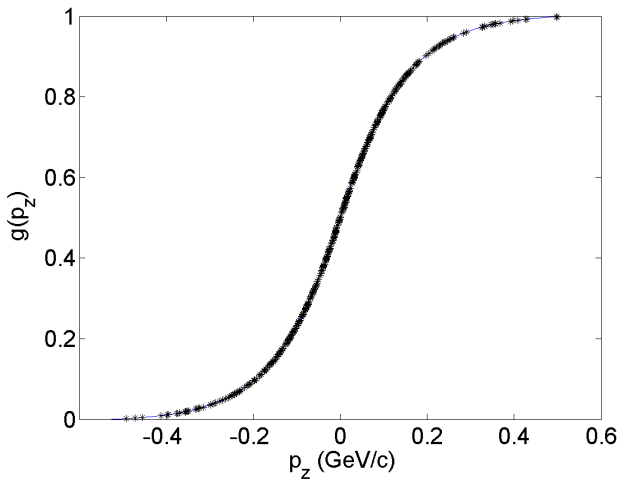


Figure 5.1: The cumulative Jüttner distribution function of momentum $g(p_z)$ for a pion gas. The red line shows the calculated cumulative function, whereas the green dots show the randomly generated 500 momenta corresponding to the randomly generated numbers ranging from 0 to 1. The temperature is $T = 100$ MeV and the chemical potential is zero.

## 5.2 Extended source, or many sources

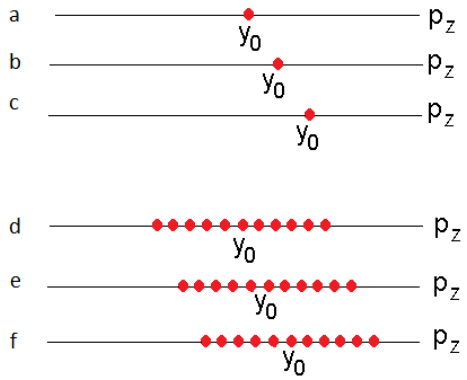


Figure 5.2: The top figure shows a single source with different source boost rapidities $y_0$. The second figure shows 11 individual sources equally spaced, but the common boost rapidity may still change.

Now, if we want to know what is the detector response to a combined source like this if we boost it by $y_{cm}$, then we need to repeat this method for all boost rapidities from -0.5 to +0.5 as shown on Fig. 5.2. This is a much more demanding calculation, but as more momenta are generated, we obtain a better statistical average which is much less affected by random numerical fluctuations.

## 5.3 TPC $\Delta y_{CM}$ calculations

As explained in chapter 2, the pseudorapidity of the sources and of each pion is calculated from the momentum following this formula:

$$\boxed{\eta = \frac{1}{2}\log\frac{|P| + P_z}{|P| - P_z} = \ln(\cot\frac{\phi}{2}) = \arctan v_z} \tag{5.1}$$

The TPC does not detect particles where $|\eta| > 0.9$ [8]. Then only the particles with $|\eta| < 0.9$ are counted and contribute to the center of mass pseudorapidity $\eta_{cm}$.

## 5.4 ZDC $\Delta y_{CM}$ calculations

These following paragraphs are based on [10] and on an unpublished work in progress [4]. At the considered LHC Pb+Pb reaction, the beam rapidity is $y_0 = 7.986$, the energy per nucleon is $\epsilon_N = 1.38$ TeV, and the total energy of the whole system with participants and spectators is $E_{tot} = A_{tot}\epsilon_N = 208 \times$

2.76 TeV. At these high energies the momentum of the spectators is the same as their energy with rather good approximation, $|E_a| = |M_a|$ *and* $|E_c| = |M_c|$. Furthermore the energy and momentum conservation gives then the energy and momentum of the participants, $E_b$ and $M_b$, as [10]:

$$\begin{aligned} E_b &= A_b\, m_{B\perp}\, \cosh(y^B) = E_{tot} - E_a - E_c\ , \\ M_b &= A_b\, m_{B\perp}\, \sinh(y^B) = -(M_a + M_c) \end{aligned} \tag{5.2}$$

where $A_b = A_{tot} - A_a - A_c$ is the net baryon number of the participants, where from the baryon charge of the original colliding nuclei, $A_{tot} = 2A_{Pb} = 208 + 208 = 416$, we subtract the net baryon charge of projectile and target spectators, $A_a$, $A_c$, $E_a$ and $E_c$ can in principle be measured by the ZDCs. Then using

$$E_{tot} = 2A_{Pb}\, m_N\ \cosh(y_0)\ \ and\ \ m_N = 938.8\ MeV/c^2\ ,$$

and dividing the second of eq. (5.2) by the first we can determine the rapidity of the participant subsystem $B$. As the total rapidity of the spectators should cancel each other out, the rapidity of subsystem B should equal the rapidity of the participant system [10].

$$y_E^{CM} \approx y^B = \left( \frac{M_a + M_c}{E_{tot} - E_a - E_c} \right)\ . \tag{5.3}$$

Ref [18] gives the same relation, but only by assuming that the fluctuations of the number of participant is negligible compared to the total number of participants.

At these high rapidities, $M_a = E_a$ and $M_c = -E_c$, so we can get the C.M. rapidity of the participant system $y^B$. If the two spectator residues would have identical energy this rapidity would be zero, but as mentioned above, due to EbE fluctuations this identity is only true on the average and not for each event.

### 5.4.1 Method

The problem is that the ZDCs detect only neutrons from the spectator fragments, and this is significantly less than the real energy and momentum of the spectators. Furthermore, pre-equilibrium emitted high energy particles will not be part of the participant system. Still we can assume that the energy measured by the ZDCs is approximately proportional with the real energy of the spectators.

To estimate the effect of this detector sensitivity, let us analyse events at a fixed impact parameter or in a given centrality bin. As an example assume that the impact parameter is $b = 0.5 b_{max} = R_{Pb}$. Then assuming a sharp nuclear surface and sharp cut between spectators and participants (similarly to the Glauber model), the system size is $A_{tot} = 416$, the size of

the participant subsystem is $A_b = 176$, while on the average the sizes of spectators are $< A_a >=< A_c >= 120$. The energy is divided among the subsystems according the same ratios.

However, due to random fluctuations the sizes of projectile and target spectators may fluctuate around these averages, together with the corresponding spectator energies and momenta, which lead to event by event c.m. rapidity changes for the participant system.

How large are these spectator size fluctuations and the corresponding c.m. rapidity fluctuation is a physical question. If there would be no size fluctuation, there would not be rapidity fluctuations either. As mentioned in the introduction to this chapter, we chose to use center of mass rapidity fluctuations between -0.5 and +0.5.

Using the geometric consideration $E_b = E_{tot} - E_a - E_c$ we can directly obtain the c.m. rapidity from the measured energies, $E_a$ and $E_c$, from eq. (5.3), as well as we can obtain $E_a$ (and $E_c$), if $y_E^{CM}$ is known.

Defining the argument of arth in eq. (5.3)

$$x = \frac{E_a - E_c}{E_{tot} - E_a - E_c} \tag{5.4}$$

and knowing $E_b$ from geometric considerations for a given impact parameter we get the spectator energies as

$$\begin{aligned} E_a &= \frac{1}{2}\left[E_{tot} + (x-1)E_b\right], \\ E_c &= E_{tot} - E_b - E_a \ . \end{aligned} \tag{5.5}$$

At the same time from

$$y_{\rm cm} = \mathrm{arth}(x) = \frac{1}{2}\ln\frac{1+x}{1-x}$$

we get that $e^{2y_{\rm cm}} = (1+x)/(1-x)$ and then

$$x = \left[e^{2y_{\rm cm}} - 1\right] / \left[e^{2y_{\rm cm}} + 1\right] \ .$$

Thus we can insert $x$ into equation (5.5) and we can get the energies $E_a, E_c$ for a given $y_{\rm cm} = y_E^{CM}$.

This way we can generate an ideal sample for $\{y_{cm}, E_a, E_c\}$ event by event. For this sample one could recover the original $< y_{cm} >$ and its variance, and the corresponding spectator energies $E_a, E_c$, which would then correspond to the total energies of spectators at points $a$ and $c$.

Thus, this way the ZDCs would represent an ideal LAD.

The detectors, however, measure smaller energies both due to detector acceptance and due to the not-measured protons and charged nuclear fragments.

### 5.4.2 ZDC detector limitations

We can simulate this effect, by taking the original ideal sample $\{y_{cm}, E_a, E_c\}$ which corresponded to a set of $\{y_{cm}\}$ values, and generate another sample $\{E'_a, E'_c\}$ by considering the acceptance of the ZDCs. These events would show smaller observed energies, $\{E'_a, E'_c\}$ which would lead to reduced $y_{cm}$ values.

If $E_a$ and $E_b$ are attenuated by a factor of $q$, the $E'_a = qE_a$ and $E'_b = qE_b$. Equation 5.4 then becomes:

$$x' \equiv \frac{q(E_a - E_c)}{E_{tot} - q(E_a + E_c) < qx}$$

$$\Rightarrow y^{CM}_{ZDC} = y'_{CM} < y_{CM}$$

Table 1 in [10] gives a detailed overview of the ZDC detector performance for the whole range of impact parameters. As we have assumed above a semi-peripheral collision with $b = 0.5 b_{max} = R_{Pb}$, and according to this table, the number of single neutrons arriving at the ZDC detector is 32.6, out of a total 77.6 participant neutrons. Taking into account that only 126 of the 208 nucleons of the Pb ion are neutrons, and assuming that each nucleon carries the same amount of energy, we find that only 25% of the total energy of the spectators is detected by the ZDC!

Assuming $q = 0.25$ and inserting equation 5.2 into equation 5.3 , we get

$$\boxed{y^{CM}_{ZDC} \approx \text{arth}\left(\frac{0.25 \cdot \delta A m_{B\perp} \cosh(y^B)}{E_{tot} - 0.25 \cdot (A_a + A_c)\ m_{B\perp}\ \sinh(y^B)}\right)} \tag{5.6}$$

## 5.5 Results

Using equation 5.6 for $y^{CM}_{ZDC}$ and equation 5.1 for $\eta^{CM}_{TPC}$ as well as the simulation methods described in section 5.3 and 5.4, we can trace the center of mass rapidity/pseudorapidity for the different detectors. We have also traced $y^{CM}_{LAD}$, which is the rapidity as it would be measured by an Large Array Detector, that is an ideal detector with no rapidity cut that measures all type of particles. It is interesting to compare $y^{CM}_{ZDC}$ and $\eta^{CM}_{TPC}$ to $y^{CM}_{LAD}$ to see how distorted the results are from the detector limitations

### 5.5.1 Simulation of detected C.M. (pseudo)-rapidities vs C.M. rapidity

Figure 5.3 shows the predicted detection of rapidity and pseudorapidity for the ZDC, the TPC and an ideal LAD versus the actual $y_{CM}$ of the distribution, for a single thermal source of $T = 0.1$ GeV emitting 500 pions

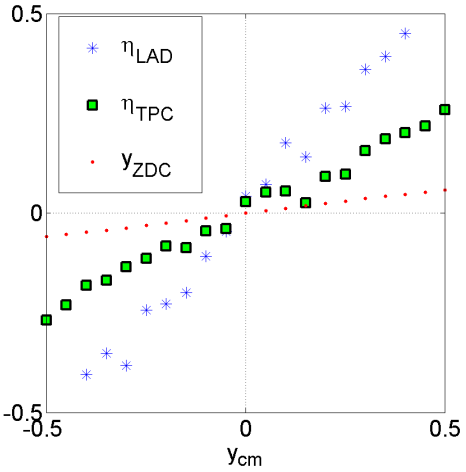


Figure 5.3: C.M. rapidity and pseudorapidity simulated measures from the ZDC, the TPC and an ideal LAD versus the actual $y_{CM}$ of the distribution, for a single thermal source of $T = 0.1$ GeV emitting 500 pions following the Jüttner distribution

following the Jüttner distribution explained in section 2.2.2. As expected, we see that the ideal LAD measures closely follows the $y_{CM}$ values, as the LAD measures the rapidity of all particles and has no cut in the rapidity range.

The TPC on the other hand only detects a fraction of the particles and will then underestimate the C.M. pseudorapidity. We observe that the gap between $\eta_{TPC}^{CM}$ and $y_{LAD}^{CM}$ increases with increasing C.M. rapidity, as for higher C.M. rapidities there will be more pions with an individual rapidity exceeding 0.9, and thus not detected by the TPC. In order to analyse this effect more closely, we have also plotted in figure 5.4 the number of pions that are detected by the TPC for different C.M. rapidities. We see that the multiplicity detected is at a maximum at $y_{CM} = 0$ but decreases rapidly for increasing $|y_{CM}|$.

Back to figure 5.3, we see that the $y_{ZDC}^{CM}$ is by far the detector that underestimates the most the C.M. rapidity. This is according to the fact that the ZDC only measures a fraction of the particles from the collision, as thoroughly explained in section 5.4.

The fluctuations on the graphs in figure 5.3 are a result of numerical random fluctuations, as the momentum of the particles was generated according to the method described in section 5.3. In order to minimize these fluctuations we have also simulated an extended source, or many sources, also explained in 5.3. Here we have simulated a source extending over 0.2 rapidities, emitting in total 10 times 500 pions. The result can be observed

in figure 5.5. As there are 10 times more particles generated, the random numerical fluctuations cancel each other out and the curves are therefore much smoother. The trace of $\eta_{TPC}^{CM}$ is now shown to saturate at higher $y_{CM}$, as when $y_{CM}$ increases, many of the new rapidities that are generated will exceed the TPC detection limit of As $|y_{cm}| < 0.9$. The TPC detector is therefore showing a non-linear distortion.

From this trace we roughly estimate the relation between the three different measures for small C.M. fluctuations as

$$\eta_{TPC}^{CM} \approx \frac{1}{5} y_{ZDC}^{CM} \approx \frac{1}{2} y_{LAD}^{CM}$$

.

These relations will of course change as the C.M. rapidity increases. The conclusion of this study is that if the physical limitations of the detectors are not taken into account, then the measured $y_{cm}$ will be underestimated.

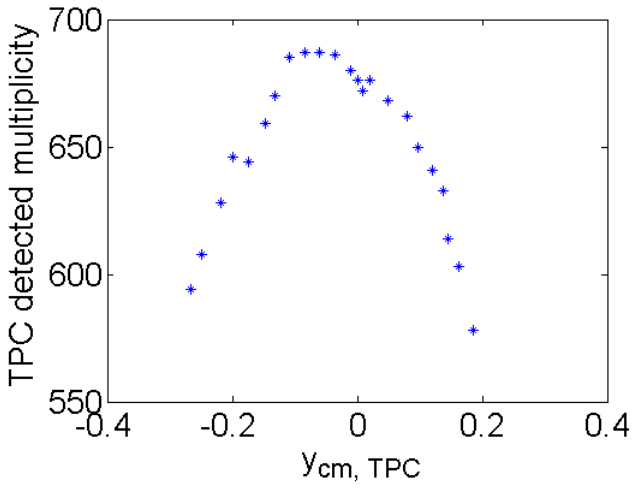


Figure 5.4: Number of pions from a thermal source described by the Jüttner distribution with a source temperature of $T = 0.1$GeV and a source rapidity $y_{CM}$. In total 500 particles are generated randomly following this distribution and the number of particles falling in the acceptance range of the TPC decreases with increasing $yCM$.

### 5.5.2 ZDC C.M. rapidity vs TPC C.M. pseudorapidity

As we need to be able to compare our data with experimental results, we have also included a trace of $y_{ZDC}^{CM}$ vs $\eta_{TPC}^{CM}$, as it should be possible to make this trace from experimental measures from the TPC and ZDC detectors.

This trace is found in figure 5.6, and shows a non-linear relation between the two detectors. This can be explained by the saturation of the TPC measures for higher $y_{CM}$ values.

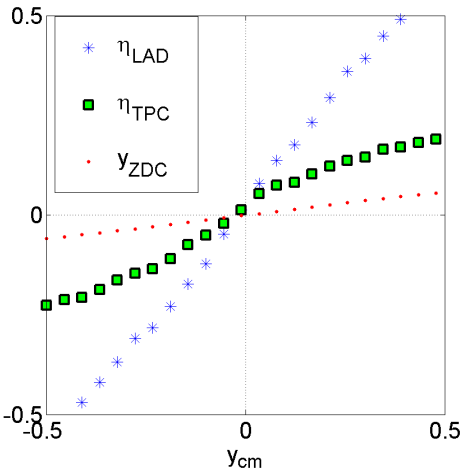


Figure 5.5: The pseudorapidity $\eta_{CM}$ of the center of mass of 500 randomly generated pions from 10 thermal sources ranging over 0.2 rapidities at $T = 0.1$GeV vs the source boost rapidity. Contrary to the case for only one source, there are now more emitted and therefore more detected particles, and much of the random fluctuations cancel each other out.

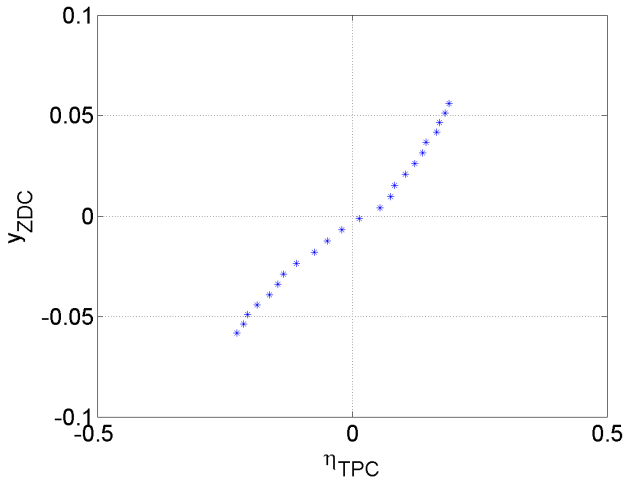


Figure 5.6: The correlation between $\eta$ as measured by the TPC with an acceptance range of $|\eta| < 0.9$ and $\eta$ as measured by the ZDC without any cut, for 10 thermal sources of $T = 0.1$ GeV each with an individual boost rapidity uniformly distributed in the range $y \in [-0.5, 0.5]$.

# Chapter 6

# Conclusion and outlook

In this thesis we have studied different aspects of heavy ion collisions, focusing on the analytical and semi-analytical calculations of the flow components $v_1$ and $v_2$ and on the TPC and ZDC detector limitations in the ALICE detector at the LHC, CERN.

Regarding the rapidity dependence of the global collective flow component $v_1$, we predict that it will no longer peak at negative rapidities for the LHC energies, due to the rotational effect from the initial angular momentum of the system. However, this will be overshadowed by initial state fluctuations of the center of mass rapidity that appear as the positions of the nucleons fluctuate in the transverse plane. Analysing the odd and even components of the function $v_1^s$, we separated the contribution on $v_1$ from the global flow and from random initial state fluctuations.

For the TPC and ZDC measures of the C.M. rapidity and pseudorapidity, we found that the detector distortions have to be taken into account to avoid underestimating the measures. It will be interesting to compare our graph showing $y_{CM}^{ZDC}$ vs $y_{CM}^{TPC}$ to experimental data from the ALICE collaboration.

During my year as a master student, I have gained insight into the physics behind and the experiments surrounding Heavy Ion Collisions. I have approached this field using analytic calculations, but also I have understood how important it is to include real life limitations into the theoretical framework. In the calculations of the collective flow components I studied the effect of initial state fluctuations, and in the simulation of the C.M. rapidity detection by the TPC and ZDC, I had to take into account the detector physical properties.

Interesting areas for further investigation would for example be to do the same simulations but for different impact parameters than $b = 0.5b_{max}$. It would also be interesting to change the distribution function, to take into account hadronization before the Freeze Out hypersurface.

# Bibliography


[1] S. Bethke, *Experimental Tests of Asymptotic Freedom*, Prog. in Part. and Nucl. Phys., (2007)

[2] L. P. Csernai, V. K. Magas, H. Stcker, and D. D. Strottman , *Fluid dynamical prediction of changed v1 flow at energies available at the CERN Large Hadron Collider*, Phys. Rev. C 84, 024914 (2011)

[3] L.P. Csernai, A.M. Skålvik, D.J. Wang, V.K. Magas H. Stcker, D.D. Strottman, Y. Cheng, Y.L. Yan, *Flow Components and initial state CM fluctuations*, Acta Physica Polonica B No 4, Vol. 43 (2012)

[4] L. P. Csernai, A. M. Skålvik, *Work in progress* (2012)

[5] L.P. Csernai: *Introduction to relativistic heavy ion collisions*, J. Wiley & Sons Ltd. (1994).

[6] Yun Cheng, L.P. Csernai, V.K. Magas, B.R. Schlei, D. Strottman, *Matching Stages of Heavy Ion Collision Models*, arXiv:1006.5820v1 [nucl-th] (2010)

[7] ALICE collaboration, *The Large Hadron Collider*, CERN (2008), available at http://public.web.cern.ch/public/en/LHC/LHC-en.html

[8] ALICE collaboration, *ALICE Time Projection Chamber*, CERN (2008), available at http://aliceinfo.cern.ch/TPC/

[9] ALICE collaboration, *The ALICE Zero Degree Calorimeters*, CERN (2008), available at http://aliceinfo.cern.ch/Public/en/Chapter2/Chap2_ZDC-en.html

[10] L.P. Csernai, G. Eyyubova, V.K. Magas, *New method for measuring longitudinal Fluctuations and directed flow in ultrarelativistic heavy ion reactions*, arXiv:1204.5885v1 [hep-ph], (2012)

[11] S. Zschocke, S. Horvat2, I. N. Mishustin, L.P. Csernai, *Non-equilibrium hadronization and constituent quark number scaling*, arXiv:1102.2310v1 [hep-ph] (2011)

[12] K. Aamodt et al. [The ALICE Collaboration], *Elliptic Flow of Charged Particles in Pb-Pb Collisions at* $\sqrt{s_{NN}} = 2.76$ *TeV*, Phys. Rev. Lett. 105, 252302 (2010).

[13] L.P. Csernai, G. Eyyubova, V.K. Magas, *New method for measuring longitudinal fluctuations and directed flow in ultrarelativistic heavy ion reactions*, arXiv:1204.5885v1 [hep-ph] (2012)

[14] L. P. Csernai, D. Röhrich, *Third flow component as QGP signal*, Phys. Lett. B 458, 454 (1999)

[15] B. Bäuchle et al., *Fluid dynamics as a diagnostic tool for heavy-ion collisions* J. Phys. G 34, s1077 (2007)

[16] P. Danielevicz and G. Odyniecz, *Transverse momentum analysis of collective motion in relativistic nuclear collisions*, Phys. Lett. B 157, 146 (1985)

[17] G. Wang, et al., (STAR Coll.), *Incident-energy and system-size dependence of directed flow* , J. Phys. G 34 s1093, (2007)

[18] Y. Cheng, Y.L. Yan, D.M. Zhou, X. Cai, B.H. Sa, L.P. Csernai, *Longitudinal Fluctuations in Partonic and Hadronic Initial State*, Phys. Rev. C 84, 034911 (2011).

[19] W. H. Press et Al, *Numerical Recipes, p 206-208*, Cambridge University Press (1986)

# Appendix A

# Publication

# FLOW COMPONENTS AND INITIAL STATE CM FLUCTUATIONS*

L.P. Csernai[a,b,c], A.M. Skålvik[a], D.J. Wang[a], V.K. Magas[d]
H. Stöcker[c], D.D. Strottman[a,c], Y. Cheng[e], Y.L. Yan[f]

[a]Institute of Physics and Technology, University of Bergen
Allegaten 55, 5007 Bergen, Norway
[b]MTA-KFKI, Research Institute of Particle and Nuclear Physics
1525 Budapest, Hungary
[c]Frankfurt Institute for Advanced Studies — Goethe University
60438 Frankfurt am Main, Germany
[d]Departament d'Estructura i Constituents de la Matèria
Universitat de Barcelona, 08028 Barcelona, Spain
[e]Institute of Particle Physics, Huazhong Normal University
430079 Wuhan, China
[f]China Institute of Atomic Energy
P.O. Box 275 (18), 102413 Beijing, China

*(Received December 5, 2011)*

At the LHC, the strong collective flow is observed in Pb+Pb collisions, as shown by the azimuthal correlations in the transverse-momentum distributions of the produced particles. We calculate flow components in a relativistic fluid dynamical model at constant time freeze out (FO) for massless equilibrated post FO pion gas. Our results indicate that at the LHC the $v_1$ flow is expected to peak at forward rapidities, at the same side and direction as the projectile residue. The effect of initial state center-of-mass rapidity fluctuations is taken into account. In order to better study the transverse-momentum flow dependence, we suggest a new "symmetrized" $v_1^{\mathrm{S}}$ function; and we also propose a new method to disentangle global $v_1$ flow from the contribution generated by the random fluctuations in the initial state. The result is sensitive to the global initial state, where different parameterizations exist.

DOI:10.5506/APhysPolB.43.803
PACS numbers: 12.38.Mh, 25.75.–q, 25.75.Nq, 51.20.+d

* Presented at the Conference "Strangeness in Quark Matter 2011", Kraków, Poland, September 18–24, 2011.

The strong elliptic flow effect was indicated by the LHC heavy ion experiments [1]. This effect exceeded the results obtained by the former lower energy measurements. Strong equilibration and thermalization phenomenon was expected to arise in the collisions. The directed flow $v_1$ was also measured by ALICE six months later [2].

RHIC and LHC results indicate that the flow has two origins [2, 3]: *(i)* the global collective (GC) flow correlated with the reaction plane of the event (EP), and *(ii)* the random fluctuation (RF) flow of all $v_n$ varieties, where the corresponding symmetry axes (*e.g.*, for $v_1$ and $v_3$) have no correlation with the reaction plane EP, instead they are observed with respect to a participant plane (PP) event-by-event (EbE) [4,5]. The participant planes are different for the neighboring flow harmonics.

Here, we discuss the behavior of the first type, *(i)*, of these flow phenomena, the GC flow, which is the weakest at RHIC and LHC energies. We will also discuss, how to separate the global $v_1$ flow, from the one produced by EbE RFs of the initial state, *(ii)*. Fluctuations, which do not follow the required symmetries can be removed, but this may not be sufficient. If we know the general features of fluctuations, this may help. If we know the features of some well defined disturbing effects, we might exploit this to our advantage.

Collective global flow in non-central collisions leads to the asymmetric azimuthal distributions, quantified by the functions $v_n(y, p_\mathrm{t})$ in the expansion

$$\frac{d^3N}{dydp_\mathrm{t}d\phi} = \frac{1}{2\pi}\frac{d^2N}{dydp_\mathrm{t}}\left[1 + 2v_1(y,p_\mathrm{t})\cos(\phi) + 2v_2(y,p_\mathrm{t})\cos(2\phi) + \cdots\right], \tag{1}$$

where $y$ is the rapidity, $p_\mathrm{t}$ is the transverse momentum, and $\phi$ is the azimuthal angle in the transverse plane with respect to the impact parameter vector, $\vec{b}$. The observed large $v_2(p_\mathrm{t})$ has important consequences. It indicates that QGP is strongly interacting and, at the same time, it also indicates that QGP is a nearly perfect fluid with minimal shear viscosity at the phase transition point [6, 7].

In a recent perfect-fluid dynamical model calculation [8], with small numerical viscosity and dissipation (see Fig. 1), we have shown that the energy density distribution in the reaction plane, 6–8 fm/$c$ after the formation of fluid dynamics, is strongly rotated with respect to the initial configuration, due to the large initial angular momentum, so that the direction of strongest transverse expansion points to $\Theta = 75°(255°)$. Thus, the upward moving matter is moving now forward and the downward moving matter backward, in contrast to what happens at RHIC and SPS energies. The substantial angular momentum is most visible at large impact parameters, $b > 0.6\, b_\mathrm{max}$, or for centrality exceeding 50%.

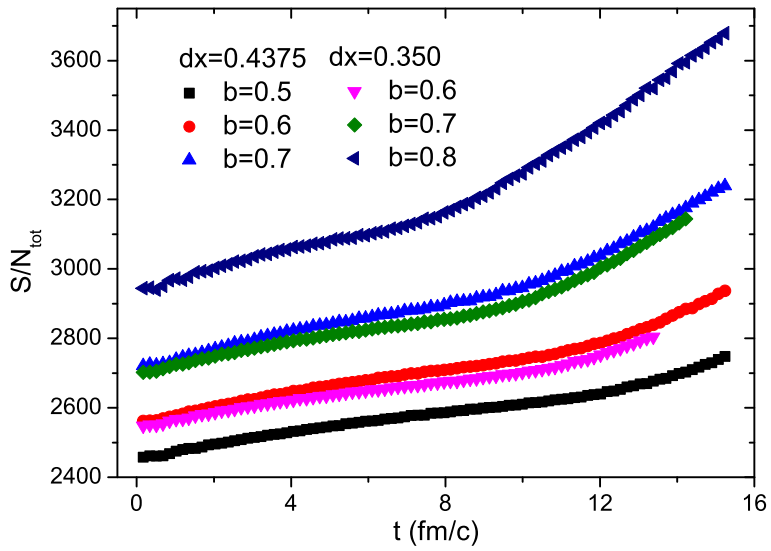


Fig. 1. The entropy per baryon estimated in the fluid-dynamics (FD) model with the cell sizes $dx = 0.4375$–$0.35\,\mathrm{fm}$, and different impact parameters $b = 0.5$–$0.8\,b_{\max}$. The value of entropy per baryon increases with larger cells, because the numerical viscosity is larger in bigger cells. At late stages ($t > 8$–$10\,\mathrm{fm}/c$) the matter is dilute; in a large part of the volume the pressure vanishes and the applicability of the FD approach gradually ceases.

In the simplest approach, we assume a constant time FO hypersurface. The transition from pre FO QGP to post FO ideal massless pion Jüttner gas is calculated according to the method described in Ref. [9], satisfying the conservation laws. In this way, for each fluid cell, $i$, we obtain a post FO flow velocity, $\vec{v}^{\,i} = (\vec{v_{\mathrm{t}}}^{\,i}, v_z^i)$, and temperature, $T^i$, as parameters of the gas. We calculate the flow observables from the contribution of these post FO contributions cell by cell.

The flow parameters, for example $v_2$, can be calculated from the final post FO distribution by the Cooper–Frye formula. Assuming a constant time FO hypersurface, we obtain simple expressions for final observables, following the arguments of Refs. [10, 11]. Thus the expression for the transverse momentum dependence of the flow is

$$v_n\left(p_\perp\right) = \frac{\sum\limits_{i=1}^{N} V_i A_i B\left(i, m_\perp^i\right) I_n\left(\gamma^i v_\perp^i p_\perp / T_i\right) \cos n\phi_0^i}{\sum\limits_{i=1}^{N} V_i A_i B\left(i, m_\perp^i\right) I_0\left(\gamma^i v_\perp^i p_\perp / T_i\right)}\,, \tag{2}$$

where

$$A_i = \frac{1}{(2\pi\hbar)^3} \exp\left(\frac{\mu^i}{T}\right) = \frac{n_i}{4\pi m^2 T_i K_2(m/T_i)}\,,$$

$\mu^i$ is the chemical potential of the given particle type in the cell $i$, $n_i$ is the density in the cell, $u_i^\mu$ is a cell flow 4-velocity: $u_i^\mu = \gamma^i(1, v_x^i, v_y^i, v_z^i) = \gamma^i(1, \boldsymbol{v}_\perp^{\boldsymbol{i}}, v_z^i)$, $m_\perp^2 = m^2 + p_\perp^2$, and $T_i$ is a temperature of the given cell. Furthermore,

$$B(m_\perp) = \frac{2m_\perp}{\sqrt{1-v_z^2}} K_1\left(\frac{\gamma m_\perp \sqrt{1-v_z^2}}{T}, \frac{\gamma m_\perp}{T}\right) - \frac{2m_\perp |v_z| e^{-\frac{\gamma p_\mathrm{t}}{T}}}{1-v_z^2},$$

where $K_n(z,w) = \frac{2^n n!}{(2n)!} z^{-n} \int_w^\infty dx (x^2 - z^2)^{n-1/2} e^{-x}$ is the modified Bessel function of the second kind.

The calculated $v_2(p_\mathrm{t})$ distributions are similar to the experimental trends both in the magnitude and the centrality dependence. The $p_\mathrm{t}$-dependence is also similar, especially at the smaller centralities.

As $v_1$ is an antisymmetric function of $y$, the $y$-integrated $v_1(p_\mathrm{t})$ value must vanish. In our calculation this is realized to an accuracy better than $10^{-16}$. Considering this obvious asymmetry, we propose to construct a symmetrized function, $v_1^\mathrm{S}$, reversing the $\vec{p}_\mathrm{t}$ direction of backward going ($y < 0$) particles. In this way, we get a non-vanishing $v_1^\mathrm{S}(p_\mathrm{t})$ function, which will be less sensitive to the initial state fluctuations,

$$v_1^\mathrm{S}(p_\perp) = \frac{\sum_i^{\text{cells}} 2D\left(\vec{v}^{\,i}, T^i, p_\perp\right) I_1\left(\gamma^i v_\mathrm{t}^i p_\perp / T^i\right) \cos\left(\phi_0^i\right)}{\sum_i^{\text{cells}} B\left(\vec{v}^{\,i}, T^i, p_\perp\right) I_0\left(\gamma^i v_\mathrm{t}^i p_\perp / T^i\right)}, \tag{3}$$

where $D(\vec{v}, T, p_\perp) = e^{-\gamma p_\perp / T} \frac{v_z}{1-v_z^2} \frac{T}{\gamma}$. The $v_1^\mathrm{S}(p_\perp)$ parameter calculated in this way is shown in Fig. 2.

The ALICE team has made a symmetry analysis of the $v_1$ flow components. The *even* and *odd* rapidity combinations gave almost identical $v_1(p_\mathrm{t})$ distributions [2], indicating that the global azimuthal symmetry does not influence the measured data, thus the measured azimuthal asymmetry must originate from random initial fluctuations. These results were based on data with 0–80% centrality percentage, where the central and semi-central collisions may show azimuthal fluctuations, which originate exclusively from random fluctuations. However, we can gain information about the $p_\mathrm{t}$ dependence of the global directed flow, if we repeat the same analysis, *i.e.*, we make separation into *even* and *odd* components, for the $v_1^\mathrm{S}(p_\mathrm{t})$ function introduced above in Eq. (3).

We have also evaluated the rapidity dependence of the $v_1$ flow component. Due to the sufficiently strong rotation of the initial state at the present LHC energy, the earlier "anti-flow" peak rotates forward, before the expansion overwhelms the rotation effect, and so the $v_1$ flow peak appears at small, but forward rapidities.

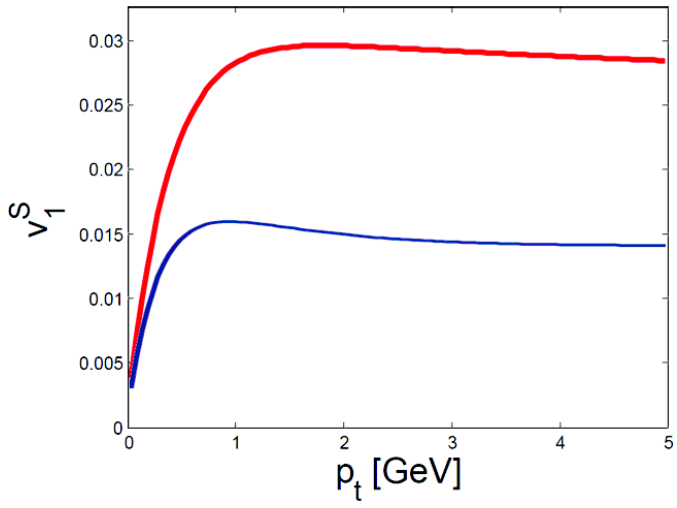


Fig. 2. The $v_1^{\mathrm{S}}$ parameter calculated for the ideal massless pion Jüttner gas, *versus* the transverse momentum $p_{\mathrm{t}}$ for $b = 0.5\,(0.7)\,b_{\mathrm{max}}$ at the FO time $t = 10\,(8)$ fm/$c$, shown as the thin/blue (thick/red) line. The magnitude of $v_1^{\mathrm{S}}$ is increasing with the impact parameter and it is about 3% at $b = 0.7\,b_{\mathrm{max}}$.

The calculated $v_1$ parameter *versus* the rapidity $y$ is shown in Fig. 3. As we can see the $v_1$ is relatively large and easily measurable in the experimental rapidity range $|y| \leq 0.8$, reaching a peak of 26% at $y = \pm 0.5$. The most important change with respect to the similar simulations for RHIC [13] is that the $v_1$ now peaks in forward direction, *i.e.*, the positive (negative) peak appears now at positive (negative) rapidity.

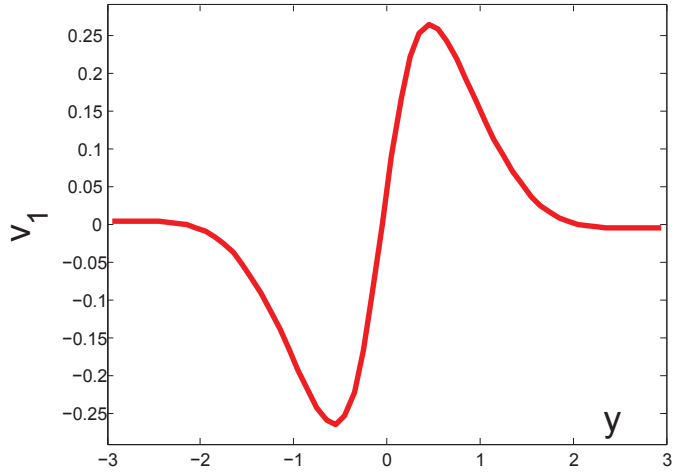


Fig. 3. The $v_1$ parameter calculated for ideal massless pion Jüttner gas *versus* the rapidity $y$ for $b = 0.7 b_{\mathrm{max}}$ at $t = 8\,\mathrm{fm}/c$ FO time. The curve represents semi analytical calculations. The $v_1$ peak appears at positive rapidity, in contrast to lower energy calculations and measurements. This is a consequence of the stronger rotation of the expanding system at higher beam energy.

At lower energies, in the same FD model calculations we obtained that the $v_1$ peaks in the backward direction (*3rd-flow component*) [12, 13], with a magnitude of about 5% and 2–3% for 158 and $65 + 65A$ GeV energies, respectively. The position of the peaks also moved from $|y| \approx 1.5$ to $|y| \approx 0.5$ with the energy increasing from SPS to RHIC. Experimentally, the 3rd-flow component was indeed measured at these energies [12, 14], although the peak values were smaller. Especially at the RHIC energies, where the highest values were $v_1 \approx 0.6\%$ and 0.2% for for $65 + 65$ and $100+100A$ GeV energies, respectively. The peaks appeared at $|y| \approx 1$ around the far end of the acceptance of the central TPC. Thus, at RHIC the $v_1$ magnitude was about 5 times smaller than the FD prediction. Also, the move towards the more central rapidities was weaker in the experiment than in FD calculations.

The reason for such a disagreement is the effect of initial state fluctuations, which may be decisive in the case of $v_1$ due to the sharp change around $y = 0$.

Initial state fluctuations may arise from the event-to-event fluctuations of nucleon positions in the transverse, participant plane. Fluctuations may also arise from individual nucleon–nucleon collisions in an event, so that even if a projectile nucleon is within the transverse domain of participants, it may not collide with any of the target nucleons, and may not become a participant. The effect of these fluctuations on different flow component has been recently analyzed, see for example [15, 16].

In both cases, the experimental cuts on the rapidity range lead to an increase of the asymmetry. Now, it should not be forgotten that $v_2(p_t)$ and $v_1^S(p_t)$, constructed from the observables within the limited rapidity range, will be affected by the initial CM rapidity fluctuations. One can expect that the $v_1^S(p_t)$ will be very much reduced, because, as we have seen, the CM rapidity fluctuations smooth out the strong $v_1$ peaks at central rapidities and strongly reduce the $v_1$ magnitude to be integrated up.

Interestingly, the initial $y_{CM}$-fluctuations lead to some increase of the elliptic flow, $v_2(p_t)$, putting it in a reasonable agreement with the ALICE data [1], see Fig. 4 and, please, note that no fine-tuning was done. At the same time, $y_{CM}$-fluctuations strongly reduce $v_1^S(p_t)$. Thus, we predict for the LHC the $v_1^S(p_t)$ flow parameters to be about 0.5–1%.

Other works have addressed the directed flow problem at RHIC energies [17, 18]. In these works, the initial state was not obtained from a dynamical model but these were parameterizations based on some assumptions. The initial flow velocity distributions were taken to be longitudinal Bjorken scaling flow solutions, identical at each point of the transverse plane. The transverse mass distribution was determined based on the Glauber model, while the longitudinal distribution was parametrized in different ways and this determined the angular momentum of the of the initial configuration.

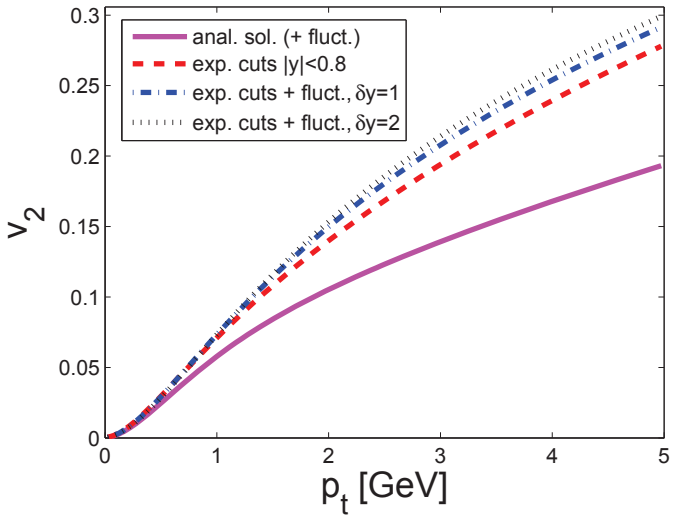


Fig. 4. The $v_2$ parameter calculated for ideal massless pion Jüttner gas, *versus* the transverse momentum $p_\mathrm{t}$ for $b = 0.7 b_\mathrm{max}$, at $t = 8\,\mathrm{fm}/c$ FO time. The magnitude of $v_2$ is comparable to the observed $v_2$ at 40–50% centrality. See the text for more explanations of different curves.

Both models gave a forward peaking directed flow for RHIC energies (where the experiments observed the anti-flow). In Ref. [18] this initial state was "tilted", and this could already reproduce the experimental anti-flow. The problem is that these parametrized states can hardly be reproduced in dynamical models starting from the pre-collision space-time configuration.

Our FD simulations of the LHC heavy ion collisions suggest that the collective directed flow $v_1(y)$ and a newly introduced $v_1^\mathrm{S}(p_\mathrm{t})$ function can and should be measured [19], although these are strongly suppressed due to initial state $y_\mathrm{CM}$-fluctuations (see Fig. 2). For the first time in hydrodynamical calculations we see that the $v_1$ global flow can change the direction to forward, in contrast to what happened at lower energies. This is a result of our tilted and moving initial state [20], in which the effective "angular momentum" from the increasing beam momentum is superseding the expansion driven by the pressure. We have also proposed a new method to distinguish contributions to $v_1(p_\mathrm{t})$ from global flow *(i)* and from random fluctuations in the initial state *(ii)*. The method is based on $v_1^\mathrm{S}(p_\mathrm{t})$ function.

## REFERENCES

[1] K. Aamodt *et al.* [ALICE Collaboration], *Phys. Rev. Lett.* **105**, 252302 (2010).

[2] R. Snellings [ALICE Collaboration], *J. Phys. G* **38**, 124013 (2011);
I. Shelyuzenkov [ALICE Collaboration], *J. Phys. G* **38**, 124167 (2011);

G. Eyyubova [ALICE Collaboration], poster at the 22nd International Conference on Ultra-Relativistic Nucleus–Nucleus Collisions (Quark Matter 2011), Annecy, France, May 23–28, 2011.

[3] B.I. Abelev *et al.* [STAR Collaboration], *Phys. Rev. Lett.* **101**, 252301 (2008).

[4] N. Borghini, P.M. Dinh, J.Y. Ollitrault, *Phys. Rev.* **C64**, 054901 (2001); J. Schukraft, presentation at the 22nd International Conference on Ultra-Relativistic Nucleus–Nucleus Collisions (Quark Matter 2011), Annecy, France, May 23–28, 2011.

[5] B. Schenke *et al.*, *J. Phys. G* **38**, 124169 (2011).

[6] P.K. Kovtun, D.T. Son, A.O. Starinets, *Phys. Rev. Lett.* **94**, 111601 (2005).

[7] L.P. Csernai, J.I. Kapusta, L.D. McLerran, *Phys. Rev. Lett.* **97**, 152303 (2006).

[8] L.P. Csernai, V.K. Magas, H. Stöcker, D.D. Strottman, *Phys. Rev.* **C84**, 024914 (2011).

[9] Yun Cheng *et al.*, *Phys. Rev.* **C81**, 064910 (2010).

[10] L.P. Csernai *et al.*, *Nucl. Phys.* **A834**, 261c (2010).

[11] P. Huovinen *et al.*, *Phys. Lett.* **B503**, 58 (2001).

[12] L.P. Csernai, D. Röhrich, *Phys. Lett.* **B458**, 454 (1999).

[13] B. Bäuchle *et al.*, *J. Phys. G* **34**, s1077 (2007).

[14] G. Wang *et al.* [STAR Collaboration], *J. Phys. G* **34**, s1093 (2007).

[15] F.G. Gardim *et al.*, *Phys. Rev.* **C83**, 064901 (2011).

[16] G.Y. Qin, H. Petersen, S.A. Bass, B. Mueller, *Phys. Rev.* **C82**, 064903 (2010); H. Petersen *et al.*, *Phys. Rev.* **C84**, 054908 (2011), [arXiv:1105.0340v2 [nucl-th]]

[17] A. Adil, M. Gyulassy, *Phys. Rev.* **C72**, 034907 (2005).

[18] P. Bozek, I. Wyskiel, *Phys. Rev.* **C81**, 054902 (2010).

[19] D. Röhrich [ALICE Collaboration], private communication.

[20] V.K. Magas, L.P. Csernai, D.D. Strottman, *Phys. Rev.* **C64**, 014901 (2001); *Nucl. Phys.* **A712**, 167 (2002).

# Appendix B

# Computer code

```
clear all
close all
clc
start=tic;

multiplicity=500;
T=0.1; % GeV
rap_extr=0.5;

%Extended source
source_length=10;
source_extrem=0.2;
source_vector=linspace(-source_extrem,source_extrem,
    source_length);
source_step=(2*source_extrem)/(source_length-1);
rapidity_vector=-rap_extr:source_step:rap_extr;
rapidity_length=length(rapidity_vector);

g=zeros(1,multiplicity);
pzi=zeros(1,multiplicity);
Pz=zeros(1,rapidity_length);
Pz_cut=zeros(1,rapidity_length);
Pt=zeros(1,rapidity_length);
Pt_cut=zeros(1,rapidity_length);
P=zeros(1,rapidity_length);
P_cut=zeros(1,rapidity_length);
length_pcut=zeros(1,rapidity_length); % Number of particles left
     after the cut for the whole source, for each rapidity

boudaries_division=200;

%% find the momentums for all possible (rapidities+source
    rapidities)
boost_vec=-(rap_extr+source_extrem):source_step:(rap_extr+
    source_extrem);
boost_length=length(boost_vec);
pzi_sum=zeros(1,boost_length); pi_sum=zeros(1,boost_length) ;
```

```
    pzi_cut_sum=zeros(1,boost_length); pi_cut_sum=zeros(1,
    boost_length) ;
34
35  for b=1:boost_length
36
37      % Fract_b(b)=(exp(2*pseudorap)-1)./(exp(2*pseudorap)+1);
38
39      boost=boost_vec(b);
40      u0=cosh(boost); ut=0; uz=sinh(boost);
41
42      pttemp_min=0;
43      pttemp_max=50;
44      pztemp_extremities=50;
45      pztemp_min=-pztemp_extremities;
46      pztemp_max=pztemp_extremities;
47
48      f = @(pz,pt)exp(-(u0*sqrt(pt.*pt+pz.*pz)-uz*pz-ut*pt)/T);
49      C_f=1/dblquad(f,pztemp_min,pztemp_max,pttemp_min,pttemp_max)
            ; %normalization
50
51      %% Calculate boundaries
52      f_min = C_f*exp(-(u0*sqrt(pttemp_min.*pttemp_min+pztemp_min
            .*pztemp_min)-uz*pztemp_min-ut*pttemp_min)/T);
53      while f_min<C_f/boudaries_division;
54          pztemp_min=pztemp_min+abs(pztemp_min)/boudaries_division
                ;
55          f_min = C_f*exp(-(u0*sqrt(pttemp_min.*pttemp_min+
                pztemp_min.*pztemp_min)-uz*pztemp_min-ut*pttemp_min)/
                T);
56      end
57
58      f_max = C_f*exp(-(u0*sqrt(pttemp_min.*pttemp_min+pztemp_max
            .*pztemp_max)-uz*pztemp_max-ut*pttemp_min)/T);
59      while f_max<C_f/boudaries_division;
60          pztemp_max=pztemp_max-pztemp_max/boudaries_division;
61          f_max = C_f*exp(-(u0*sqrt(pttemp_min.*pttemp_min+
                pztemp_max.*pztemp_max)-uz*pztemp_max-ut*pttemp_min)/
                T);
62      end
63
64      pztemp=linspace(pztemp_min,pztemp_max,multiplicity);
65
66      f_t = C_f*exp(-(u0*sqrt(pttemp_max.*pttemp_max)-ut*
            pttemp_max)/T);
67      while f_t<C_f/boudaries_division;
68          for indz=1:multiplicity
69              pz=pztemp(indz);
70              f_t(indz) = C_f*exp(-(u0*sqrt(pttemp_max.*pttemp_max
                    +pz.*pz)-uz*pz-ut*pttemp_max)/T);
71          end
72          f_t=max(f_t);
73          pttemp_max=pttemp_max-pttemp_max/5;
74      end
75      pttemp=linspace(pttemp_min,pttemp_max,multiplicity);
```

```
76
77      f = @(pz,pt)exp(-(u0*sqrt(pt.*pt+pz.*pz)-uz*pz-ut*pt)/T);
78      C_f=1/dblquad(f,pztemp_min,pztemp_max,pttemp_min,pttemp_max)
            ; %normalization with new boundaries
79      f = @(pz,pt)C_f*exp(-(u0*sqrt(pt.*pt+pz.*pz)-uz*pz-ut*pt)/T)
            ;
80
81      %% Calculate and plot the distribution function f
82      ff=zeros(multiplicity);
83      for indz=1:multiplicity
84          pz=pztemp(indz);
85          for indt=1:multiplicity
86              pt=pttemp(indt);
87              ff(indt,indz)=C_f*exp(-(u0*sqrt(pt*pt+pz*pz)-uz*pz-
                    ut*pt)/T);
88          end
89      end
90
91      %% Find g(x) numerically
92      g(2)=dblquad(f,pztemp_min,pztemp(2),pttemp_min,pttemp_max);
93      for indz=3:multiplicity
94          g(indz)=g(indz-1)+dblquad(f,pztemp(indz-1),pztemp(indz),
                pttemp_min,pttemp_max);
95      end
96
97      %% Generate pzi from g_num, the inverse of the cumulative
            distribution of f(pz)
98      ui=rand(1,multiplicity); %random number uniformly
            distributed [0,1]
99      i=1; j=2;
100
101     while i<multiplicity+1
102         if ui(i)<g(j)
103             pzi(i)=(pztemp(j)+pztemp(j-1))/2; i=i+1; j=2;
104         else
105             if j<multiplicity;  j=j+1;
106             else
107                 pzi(i)=pztemp(multiplicity); i=i+1; j=2;
108                 end
109         end
110     end
111     pzi=sort(pzi);
112     ui=sort(ui);
113
114 %     figure(8)
115 %     plot(pztemp,g,'-b')
116 %     hold on
117 %     plot(pzi,ui,'*k')
118 %     xlabel('\fontsize{20} pz')
119 %     ylabel('\fontsize{20} g(pz)')
120 %     png(['figures/g_boost',num2str(boost)])
121 %     set(gca, 'FontSize', 20)
122
123
```

```
124     %% Find dN_dpz(pzi)
125     % N= 2*pi doubleintegral ( pt * f ) dpt dpz
126     % dN/dpz = 2*pi*pt*f dpt
127     dN_dpz=zeros(1,multiplicity);
128     h=zeros(multiplicity);
129     for indz=1:multiplicity
130         pzvar=pzi(indz);
131         ptf=@(pt)C_f*pt.*exp(-(u0*sqrt(pt.*pt+pzvar.*pzvar)-uz*
                pzvar-ut*pt)/T); %  ???
132         h(2,indz)=quad(ptf,pttemp_min,pttemp(2));
133         for indt=3:multiplicity
134             ptvar=pttemp(indt);
135             ptvar_before=pttemp(indt-1);
136             h(indt,indz)=h(indt-1,indz)+quad(ptf,ptvar_before,
                    ptvar); %integrate ptf with pt
137         end
138     end
139     %     dN_dpz=h(multiplicity,:);
140     %     dN_dpz=dN_dpz/max(dN_dpz);
141     %     t_dN_dpz = toc
142     %     figure
143     %     plot(pzi,dN_dpz,'r*')
144     %     xlabel('pz')
145     %     ylabel('dN / dpz')
146
147     %% Generate pti from the inverse of the cumulative
            distribution of h
148     pti=zeros(1,multiplicity);
149     j=2;                    %j is the indice of the pttemp vector
150     indz=1;                   %Start by chosing the 1st plane (pz
            ,h) to work on
151     w=rand*max(h(:,indz));  %random number uniformly distributed
             between 0 and the max of h for that special pz!!! %%
            lurer litt p denne!!!
152
153     while indz<multiplicity
154         if w < h(j,indz)
155             pti(indz)=(pttemp(j)+pttemp(j-1))/2;
156             indz=indz+1;
157             j=2;
158             w=rand*max(h(:,indz));  %generate new w!!!
159         else
160             if j<multiplicity %If we are not yet at the end of
                    the pt vector, we go to the next pt element
161                 j=j+1;
162             else
163                 pti(indz)=pttemp_max;
164                 indz=indz+1;
165                 j=2;  % If we are at the end  of the j vector
                        and go on to a new pz plane!!!
166                 w=rand*max(h(:,indz));  %generate new w!!!
167             end
168         end
169     end
```

```
170
171     %           figure(6)
172     %           [PZ,PT]=meshgrid(pztemp,pttemp);  % VELDIG rart,
            hvis vi bytter rekkeflgen p disse blir det helt krise
            !!!!
173     %           mesh(PT,PZ,h)
174     %           xlabel('pttemp')
175     %           ylabel('pztemp')
176     %           zlabel('h')
177     %           view(0,90)
178     %           png(['figures/h/',num2str(b),' ',num2str(rap_extr)
            ,' ',num2str(source_length),' ',num2str(source_extrem)
            ,' T',num2str(T),'GeV mult',num2str(multiplicity),' h
            '])
179     %
180     %% Calculate the total momentum for all particles
181     pii=sqrt((pzi.*pzi+pti.*pti));
182     pseudorap=0.5*log((pii+pzi)./(pii-pzi));
183     pseudorap=pseudorap(find(abs(pseudorap)<99999));
184     pzi_cut=pzi(find(abs(pseudorap)<.9));  %The cutting
            condtition is that the pz of one event should be less
            than 0.8
185     pti_cut=pti(find(abs(pseudorap)<.9));
186     pi_cut=sqrt((pzi_cut.*pzi_cut+pti_cut.*pti_cut));
187
188     Efract_i=(exp(2*pseudorap)-1)./(exp(2*pseudorap)+1);
189
190     cut_length(b)=length(pzi_cut);
191
192     pzi_sum(b)=sum(pzi); pi_sum(b)=sum(pii); pzi_cut_sum(b)=sum(
            pzi_cut); pi_cut_sum(b)=sum(pi_cut);
193
194     pseudorap_cm_i=pseudorap;
195     pseudorap_cm_cut_i=0.5*log((pi_cut+pzi_cut)./(pi_cut-pzi_cut
            ));
196     pseudorap_cm_sum(b)=mean(pseudorap_cm_i(1:multiplicity-1));
197     pseudorap_cm_cut_sum(b)=mean(pseudorap_cm_cut_i);
198     Efract_b(b)=mean(Efract_i);
199
200
201     %pzi_sum(b)=mean(pzi); pi_sum(b)=mean(pii); pzi_cut_sum(b)=
            mean(pzi_cut); pi_cut_sum(b)=mean(pi_cut);
202     %% Progress bar
203     clc
204     progress=b/boost_length;
205     time_passed=toc(start);
206     min_passed=floor(time_passed/60);
207     sec_passed=time_passed-min_passed*60;
208     time_left=time_passed/progress - time_passed;
209     min_left=floor(time_left/60);
210     sec_left=time_left-min_left*60;
211     disp(['progress ',num2str(progress*100,'%4.0f'),'%, time
            elapsed ',num2str(min_passed,'%4.0f'),'m ',num2str(
            sec_passed,'%4.0f'),'s, estimated time remaining ',
```

```
        num2str(min_left,'%4.0f'),'m ',num2str(sec_left,'%4.0f'),
        's'])
212
213 end
214
215
216 %% Run through all rapidities (main loop)
217 for r=1:rapidity_length
218     length_pcut_s=zeros(1,source_length); % Number of particles
        that are left after the cut for each point of the source
219     Sz=zeros(1,source_length);            % Sum of all pzi for
        each point of the source, cumulative
220     S=zeros(1,source_length);             % Sum of all pi for
        each point of the source, cumulative
221     Sz_cut=zeros(1,source_length);        % Sum of all pzi cut
        for each point of the source, cumulative
222     S_cut=zeros(1,source_length);         % Sum of all pi cut
        for each point of the source, cumulative
223
224     for s=1:source_length
225
226 % s is the indice of the point in one extended source
227             Sz(s)=pzi_sum(s+r-1); Sz_cut(s)=pzi_cut_sum(s+r-1);
228             S(s)=pi_sum(s+r-1);   S_cut(s)=pi_cut_sum(s+r-1);
229             Pseudo(s)=pseudorap_cm_sum(s+r-1);
230             Pseudo_cut(s)=pseudorap_cm_cut_sum(s+r-1);
231             Efraction(s)=Efract_b(s+r-1);
232
233         length_pcut_s(s)=cut_length(s+r-1); % length of the cut
            pzi vector for each point of an extended source
234     end % End of source loop
235     Pz(r)=sum(Sz);
236     Pz_cut(r)=sum(Sz_cut);
237     P(r)=sum(S);
238     P_cut(r)=sum(S_cut);
239
240     PPseudo(r)=sum(Pseudo);
241     PPseudo_cut(r)=sum(Pseudo_cut);
242     Efraction_sum(r)=mean(Efraction);
243
244     length_pcut(r)=sum(length_pcut_s); % number of points left
        after cut, for each rapidity
245 end % End of rapidity loop
246
247 %% Plot figures
248 pseudorap_cm_LAD=0.5*log((P+Pz)./(P-Pz));
249 Etot=576000; % GeV
250 Npart=176; %Number of participants in the collision
251 Ntot=416; %Total number of particles (particpants+spectators)
252 Nspect=Ntot-Npart; % Number of spectators
253 y0=7.986; %Total rapidity of collision
254 mn=0.9388; %Mass of each nucleon, in GeV
255 att_fact=0.2545; %Attenuation factor, part of spectators that
    the ZDC can detect (ref table 1 in laszlos last paper)
```

```
256
257 Espect=Nspect*mn*cosh(y0);
258 dN=Npart*(tanh(rapidity_vector)/tanh(y0));
259 Ea_Ec=dN*mn*sinh(y0);
260
261 %rap_cm_ZDC=atanh(Efraction_sum);
262 rap_cm_LAD=0.5*log((cosh(rapidity_vector)+sinh(rapidity_vector))
      ./(cosh(rapidity_vector)-sinh(rapidity_vector)));
263 pseudorap_cm_TPC=0.5*log((P_cut+Pz_cut)./(P_cut-Pz_cut));
264 rap_cm_ZDC=atanh(att_fact*(Ea_Ec)/(Etot-att_fact*Espect));
265 %rap_cm_ZDC=atanh(sinh(rapidity_vector)/(Etot-0.65*Etot*factor))
      ;
266
267 save(['multisource_T',num2str(T),'_mult',num2str(multiplicity),'
      _rapidity_length',num2str(rapidity_length)])
268
269
270 close all
271
272 figure(1)
273 plot(pseudorap_cm_TPC,pseudorap_cm_LAD,'*')
274 xlabel('\fontsize{20}\eta_{\fontsize{18}TPC}')
275 ylabel('\fontsize{20}\eta_{\fontsize{18}LAD}')
276 axis([-0.5 0.5 -1 1])
277 grid on
278 set(gca, 'FontSize', 20)
279 png(['figures/multisource_TpcLad_T',num2str(T),'_mult',num2str(
      multiplicity),'_rapidity_length',num2str(rapidity_length)])
280
281 figure(2)
282 plot(pseudorap_cm_TPC,rap_cm_ZDC,'*')
283 xlabel('\fontsize{20}\eta_{\fontsize{18}TPC}')
284 ylabel('\fontsize{20}y_{\fontsize{18}ZDC}')
285 axis([-0.5 0.5 -0.1 0.1])
286 grid on
287 set(gca, 'FontSize', 20)
288 png(['figures/multisource_TpcZdc_T',num2str(T),'_mult',num2str(
      multiplicity),'_rapidity_length',num2str(rapidity_length)])
289
290 figure(3)
291 plot(rapidity_vector,pseudorap_cm_LAD,'*b','MarkerSize',10)
292 hold on
293 plot(rapidity_vector,pseudorap_cm_TPC,'s','LineWidth',2,'
      MarkerEdgeColor','k','MarkerFaceColor','g','MarkerSize',10)
294 plot(rapidity_vector,rap_cm_ZDC,'.r','MarkerSize',10,'LineWidth'
      ,3)
295 xlabel('\fontsize{20}y_{cm}')
296 %ylabel('\fontsize{20}measured \eta_{cm}')
297 legend('\fontsize{20}\eta_{LAD}','\fontsize{20}\eta_{TPC}','\
      fontsize{20}y_{ZDC}','location','NorthWest')
298 %title(['T= ',num2str(T),' GeV, multiplicity= ',num2str(
      multiplicity),' source length=',num2str(source_length),'
      source extremities=',num2str(source_extrem)])
299 axis([-(rap_extr) (rap_extr) -(rap_extr) (rap_extr)])
```

```
300 axis square
301 set(gca, 'FontSize', 20)
302 png(['figures/multisource_RapVsPseu',num2str(T),'_mult',num2str(
    multiplicity),'_rapidity_length',num2str(rapidity_length)])
303
304 figure(5)
305 plot(rapidity_vector,length_pcut,'LineWidth',2)
306 xlabel('\fontsize{20} y_{cm}')
307 ylabel('\fontsize{20} TPC detected multiplicity')
308 %title(['T= ',num2str(T),' GeV, multiplicity= ',num2str(
    multiplicity)])
309 set(gca, 'FontSize', 20)
310 png(['figures/multisource_T',num2str(T), '_mult',num2str(
    multiplicity),'_rapidity_length',num2str(rapidity_length)])
311
312 figure(6)
313 plot(pseudorap_cm_TPC,length_pcut,'*')
314 xlabel('\fontsize{20} y_{cm, TPC}')
315 ylabel('\fontsize{20} TPC detected multiplicity')
316 %title(['T= ',num2str(T),' GeV, multiplicity= ',num2str(
    multiplicity)])
317 set(gca, 'FontSize', 20)
318 png(['figures/multisource_T',num2str(T), '_mult',num2str(
    multiplicity),'_rapidity_length',num2str(rapidity_length)])
319
320 time_passed=toc(start);
321 min_passed=floor(time_passed/60);
322 sec_passed=time_passed-min_passed*60;
323 clc
324 disp(['progress 100%, total time of calculation ',num2str(
    min_passed,'%4.0f'),'m ',num2str(sec_passed,'%4.0f'),'s'])
```